



Harokopio University

School of Environment, Geography and Applied
Economics

Department of Geography

Postgraduate Program

“Applied Geography and Spatial Planning”

Course C: Geo-informatics

**Rio-Patra fault zone monitoring
using multi-temporal DInSAR
techniques**

Postgraduate thesis

Papadopoulos Alexandros

Athens, 2018



Harokopio University

School of Environment, Geography and Applied
Economics

Department of Geography

Postgraduate Program

“Applied Geography and Spatial Planning”

Course C: Geo-informatics

Three-member Committee:

Isaak Parcharidis (Supervisor)

Associate Professor, Department of Geography, Harokopio University

Panagiotis Elias

**Scientific Staff, Institute of Astronomy, Astrophysics, Space
Applications & Remote Sensing, National Observatory of Athens**

Christos Chalkias

Professor, Department of Geography, Harokopio University

Ο Παπαδόπουλος Αλέξανδρος

δηλώνω υπεύθυνα ότι:

- 1) Είμαι ο κάτοχος των πνευματικών δικαιωμάτων της πρωτότυπης αυτής εργασίας και από όσο γνωρίζω η εργασία μου δε συκοφαντεί πρόσωπα, ούτε προσβάλει τα πνευματικά δικαιώματα τρίτων.

- 2) Αποδέχομαι ότι η ΒΚΠ μπορεί, χωρίς να αλλάξει το περιεχόμενο της εργασίας μου, να τη διαθέσει σε ηλεκτρονική μορφή μέσα από τη ψηφιακή Βιβλιοθήκη της, να την αντιγράψει σε οποιοδήποτε μέσο ή/και σε οποιοδήποτε μορφότυπο καθώς και να κρατά περισσότερα από ένα αντίγραφα για λόγους συντήρησης και ασφάλειας.

Acknowledgement

First I would like to thank my thesis advisor, Assistant Professor Issaak Parcharidis of the Department of Geography at Harokopio University for his faith in me and his eagerness to help me whenever I ran into a trouble spot or had a question. Under prof. Parcharidis supervision, I had the opportunity to work on my own with estimable support and guidance.

Other than Prof. Parcharidis, I would like to thank my teammates from the Remote Sensing Team of Harokopio University of Athens for their assistance during the analysis procedure as they were willing to share their knowledge and experiences.

Moreover, I would like to express my thanks to the experts who were involved in the validation of this research project: directeur de recherche CNRS, Pierre Briole and scientific staff of IAASARS/NOA, Dr. Panagiotis Elias. Without their work on the Corinth Rift Laboratory (CRL), the validation could not have been successfully conducted.

I would also like to acknowledge the European Space Agency (ESA) for the ERS, Envisat and Sentinel-1 data provided, the German Aerospace Center (DLR) for the TerraSAR-X imagery and the National Cadastre & Mapping Agency S.A. for the precise DEM given to me.

Contents

Περίληψη	5
Abstract	6
List of Figures	7
List of Tables	10
List of Abbreviations	11
1 Introduction	13
2 Synthetic Aperture Radar basics and SAR interferometry	14
2.1 SAR system	14
2.2 SAR images	16
2.3 SAR Interferometry	16
2.3.1 Coherence of interferometric images	18
2.3.2 SAR Differential Interferometry	19
2.4 Phase unwrapping	20
2.5 Multi-temporal techniques	21
2.5.1 Interferometric stacking	21
2.5.2 Persistent Scatterer Interferometry	22
2.5.3 Small BAseLine Subset	24
2.5.4 Hybrid method with SVD	26

3	Geology	27
3.1	North-Western Peloponnese	27
3.1.1	Stratigraphy	27
3.1.2	Geo-dynamics	30
3.1.3	Neotectonics	31
3.1.4	Seismicity	32
3.2	Surface motion	34
3.2.1	Subsidence	34
3.2.2	Elevation	34
3.2.3	Strike-slip faults	35
4	Seismic Risk	36
4.1	Seismic Hazard	36
4.2	Vulnerability	37
5	Literature Review	40
6	Data	43
6.1	Digital Elevation Model	43
6.2	Synthetic Aperture Radar Observation data	43
6.2.1	ERS	44
6.2.2	ENVISAT	46
6.2.3	TerraSAR-X	50
6.2.4	Sentinel-1	51

7 Methodology	55
7.1 PSs method - IPTA algorithm	55
7.1.1 IPTA pre-processing	55
7.1.2 IPTA processing	57
7.2 Hybrid method - SVD algorithm	59
7.2.1 SVD pre-processing	59
7.2.2 SVD processing	60
8 Results	61
9 Discussion	71
10 Conclusions	73
References	74
Appendices	i
A ERS data frequencies	i
B Envisat data frequencies	ii
C TerraSAR-X data frequencies	iii
D Sentinel-1 data frequencies	iv

Περίληψη

Το θέμα αυτής της μελέτης είναι η παρακολούθηση της ζώνης ρηγμάτων στην περιοχή Πάτρα-Ρίο από το 1993 έως το 2017. Χρησιμοποιώντας διαχρονική συμβολομετρία (DInSAR), η μετατόπιση εδάφους ή κτιρίων γίνεται μετρήσιμη.

Ο κύριος στόχος της διατριβής είναι η μελέτη πιθανών γεωλογικών κινδύνων σε κοντά στην πόλη της Πάτρας. Με τη χρήση του διαχρονικού συστήματος DInSAR, οι μετατοπίσεις και η ταχύτητα τεκτονικών τεμαχών τα τελευταία 25 χρόνια έχουν παρατηρηθεί. Η μελέτη παλαιότερων τεκτονικών κινήσεων μπορεί να βοηθήσει τον δήμο να αξιολογήσει τους κινδύνους που είναι εγγενής στην τεκτονική της περιοχής για κτίρια όπως το τοπικό νοσοκομείο, το Πανεπιστήμιο της Πάτρας ή ακόμα και τα σπίτια των κατοίκων.

Προκειμένου να μελετηθεί η επιφανειακή κίνηση των 25 συνεχόμενων χρόνων, χρησιμοποιήθηκαν σύνολα δεδομένων, καθένα από τα οποία κάλυπτε διαφορετική χρονική περίοδο. Από φθίνουσες και ανερχόμενες δορυφορικές τροχιές, παρέχοντας διαφορετικές γεωμετρικές προβολής οι οποίες έχουν χρησιμοποιηθεί για την πλήρη κατανόηση της μετατόπισης εδάφους. Λεπτομερέστερα, η περίοδος από το 1993 έως το 1999 καλύπτεται από τους δορυφόρους ERS-1 και ERS-2, τα έτη 2003 έως 2010 καταγράφηκαν από το δορυφόρο Envisat-1, κατά τη διάρκεια του 2010 έως το 2012 ο TerraSAR-X συλλέγει δεδομένα και τα τελευταία χρόνια από το 2015 έως το 2017, η παρατήρηση έγινε από τους δορυφόρους Sentinel-1A και Sentinel-1B.

Η διαχρονική ανάλυση έχει επιτευχθεί μέσω του λογισμικού Gamma Remote Sensing. Αλγόριθμοι SVD και PSI έχουν χρησιμοποιηθούν για την επεξεργασία των δεδομένων. Η αξιολόγηση των αποτελεσμάτων έχει γίνει με βάση τη γνωστή τοπική γεωλογία και γεωγραφικά χαρακτηριστικά καθώς και με τις συνεχείς παρατηρήσεις GNSS της περιοχής.

Στα αποτελέσματα αυτής της εργασίας, αποδεικνύεται ότι οι πόλεις της Πάτρας και του Ρίου εδρεύουν σε περιοχές με ενεργή τεκτονική. Κίνηση εδάφους έχει καταγραφεί σε όλα τα έτη που μελετήθηκαν τόσο σε κανονικά ρήγματα, όσο και σε ρήγματα οριζόντια ολίσθησης.

Λέξεις κλειδιά: SAR συμβολομετρία, εδαφική κίνηση, ενεργή τεκτονική, οριζόντια ολίσθηση, Πάτρα-Ρίο.

Abstract

The topic of this study is the fault zone monitoring of the Patra-Rio region from 1993 to 2017. Using multi-temporal Differential Synthetic Aperture Radar Interferometry (DInSAR) techniques, displacement of soil or buildings has been identified.

The main objective of the thesis is to study possible geo-hazards in close proximity to the large city of Patras. With the use of multi-temporal DInSAR, displacements and velocity of blocks in the past 25 years have been observed. Studying former displacement may help the municipality to evaluate the risks inherent to the tectonics of the area for buildings such as the local hospital, the University of Patras or even the residents' houses.

In order to study surface motion of 25 continuous years, multiple satellites' data-sets have been used, each one covering different temporal period. Moreover, descending and ascending acquisitions, providing different viewing geometries have been used to fully understand the ground displacement. In detail, the period from 1993 to 1999 has been covered by ERS-1 and ERS-2 satellites, the years 2003 to 2010 were recorded from the Envisat-1 satellite, during 2010 to 2012 TerraSAR-X has been collecting data and the last years from 2015 to 2017, observation has been conducted by the Sentinel-1A and Sentinel-1B satellites.

The multi-temporal analysis has been achieved through the Gamma Remote Sensing Software. Single Value Decomposition (SVD) and Persistent Scatterers Interferometry (PSI) algorithms were used to process the data. The evaluation of the results has been done with the known local geology and geographical settings, as well as with the on going GNSS observations.

In the results of this thesis, it is shown that Patras and Rio cities rest on areas with active tectonics. Ground motion has been recorded through all of the studied years and other than normal faults, strike-slip faults also exist.

Keywords: SAR interferometry, ground motion, active tectonics, strike-slip, Patras, Rio.

List of Figures

1	SAR systems' geometry and terms. H_{SAR} is the height of the SAR platform, c is the velocity of the microwave, and $r(t)$ and R are the slant-range distances at the azimuth time t and when the antenna is nearest to the target at the origin of the ground coordinate system (x, y) (Ouchi, 2013).	15
2	Polarimetric radar transmitted waves: (a) Horizontally (b) Vertically (Vasile and Besic, 2013).	15
3	Unflattened (left) and flattened (right) interferogram of a portion of the Italian Alps and the Pianura Padana (Ferretti et al., 2007a).	17
4	Coherence maps from ERS images: (a) refers to a small baseline and a small temporal separation, (b) refers to very small baseline separation and temporal decorrelation (Manunta, 2009).	19
5	Modified illustration of wrapped and unwrapped phase from Van-Zyl (2017) and Veci (2016a).	21
6	Interferometric point target analysis (IPTA) processing graph (Werner et al., 2003).	24
7	Small BAseLine Subset (SBAS) processing graph (Casu, 2009).	26
8	Stratigraphic columns, modified from (Robertson and Shallo, 2000).	28
9	General geologic map with data from the (I.G.M.E., 2017).	29
10	Simplified geological map of the Rio-Antirio broader area (Parcharidis et al., 2009a).	30
11	Tectonic map of the primary active faults (Doutsos and Poulimenos, 1992).	32
12	Seismicity map of broader area of Patras, from 550 B.C to 2010. Complete data are illustrated only for the following periods and magnitudes $M > 6.5$ since 1901, $M > 5.2$ since 1911, $M > 4.8$ since 1950 and $M > 4.5$ since 1964, data from A.U.TH. (1981), processed by the author.	33
13	Diagrams of dip-slip normal and reverse/thrust faults (Girty, 2009).	35

14	Diagrams of strike-slip faults (Girty, 2009).	35
15	Smoothed probabilistic seismic hazard map of Greece and adjacent areas in terms of PGA values at 10% probability of exceedance, until 2054 (Tsapanos, 2008).	37
16	The faults demonstrated on a level-1C Sentinel-2A image, accessible from (USGS, 2017), are after the works of Flotte et al. (2005) and Koukis et al. (2005)	39
17	Map of the vertical rate of the city of Patras, using PSI/SBAS technique. The black dotted lines correspond to cross sections of original author. The main discontinuities of A-A', B until B' and to B'', at C, D, E until F ac be discriminated. The thin white dotted lines visualise the fault traces of Agia Triada and Rion-Patras fault zone (Elias, 2013).	41
18	Map of the vertical rate of the Rion-Patras fault zone, using PSI/SBAS technique. The black dotted lines correspond to cross sections of original author. The white dashed line visualises the RPfz (Elias, 2013).	42
19	Here are illustrated the used satellites' lifetime and type of band, configured from the original image Schmullius (2017)	44
20	Plots of aquisition dates versus the baselines of the interferograms.	56
	(a) ERS descending	56
	(b) ERS ascending	56
	(c) Envisat descending	56
	(d) Envisat ascending	56
	(e) TerraSAR-X ascending	56
21	Plots of aquisition dates versus the baselines of the interferograms.	60
	(a) Sentinel-1 descending	60
	(b) Sentinel-1 ascending	60

22 IPTA results for the ERS descending data-set. Values < -8 or > 8 mm/year, that consist <10% of the overall results, have been excluded. 63

23 IPTA results for the ERS ascending data-set. Values < -8 or > 8 mm/year, that consist <10% of the overall results, have been excluded. 64

24 IPTA results for the Envisat descending data-set. Values < -8 or > 8 mm/year, that consist <10% of the overall results, have been excluded. 65

25 IPTA results for the Envisat ascending data-set. Values < -8 or > 8 mm/year, that consist <10% of the overall results, have been excluded. 66

26 IPTA results for the TerraSAR-X ascending data-set. Values < -8 or > 8 mm/year, that consist <16% of the overall results, have been excluded. 67

27 SVD results for the Sentinel-1 descending data-set. Values < -8 or > 8 mm/year, that consist <10% of the overall results, have been excluded. 68

28 SVD results for the Senitnel-1 ascending data-set. Values < -8 or > 8 mm/year, that consist <10% of the overall results, have been excluded. 69

29 Distribution curves for the northern feature of PRFZ. 70

30 Distribution curves for the southern feature of PRFZ. 70

List of Tables

1	ERS-1 and ERS-2 level 1 SLC's image product characteristics (ESA, 2017a).	44
2	ERS-1 and 2 imagery (descending, track: 279, frame: 2835, polarization: VV) that has been used (in bold the master reference image).	45
3	ERS-1 and 2 imagery (ascending, track: 186, frame: 765, polarization: VV) that has been used.	46
4	ENVISAT level 1 SLC's image product characteristics (ESA, 2016).	47
5	Envisat-1 imagery (descending, track: 279, frame: 2835, polarization: VV) that has been used.	48
6	Envisat-1 imagery (ascending, track: 415, frame: 765, polarization: VV) that has been used.	49
7	TerraSAR-X, StripMap (SM), single polarization, level 1 SLC's image product characteristics (Airbus Defence and Space, 2014).	50
8	TerraSAR-X imagery (ascending, relative orbit: 161, polarization: HH) that has been used.	51
9	Sentinel-1 level 1 SLC's image product characteristics (ESA, 2017b).	52
10	Sentinel-1 imagery (descending, track: 80, frame: 463) that has been used.	53
11	Sentinel-1 imagery (ascending, track: 175, frame: 122) that has been used.	54

List of Abbreviations

ATF	Agia Triada fault
CRL	Corinth Rift Laboratory
DEM	Digital Elevation Model
DInSAR	Differential Interferometry
DLR	German Aerospace Cente
EOLi-SA	Earth Observation Link - Stand Aloner
ESA	European Space Agency
ERS	European Remote Sensing
HH	Horizontal transmit, Horizontal received
HV	Horizontal transmit, Vertical received
InSAR	Interferometric SAR
IPTA	Interferometric Point Target Analysis
LOS	Line Of Sight
LS	Least Squares
PS	Permanent Scatterer
PSI	Persistent Scatterer Interferometry
PSInSARTM ...	Permanent Scatterer InSAR
PSs	Permanent Scatterers
PU	Phase unwrapping
RPfz	Rio-Patra fault zone
S/N	signal to noise ratio

- SAR** Synthetic Aperture Radar
- SBAS** Small BAseline Subset
- SNR** signal-to-noise ratio
- SLC** Single Look Complex
- SSC** Single Look Slant range Complex
- SVD** Singular Value Decomposition
- TOPSAR** Terrain Observation with Progressive Scan SAR
- VH** Vertical transmit, Horizontal received
- VV** Vertical transmit, Vertical received

1 Introduction

Throughout history, humans have been deeply affected by natural disasters (CRED, 2015). One of the sciences able to decipher several natural disasters is geology. Earth is alive and even though the planet is more dynamic towards the center, some deformation reaches the surface (Massonnet and Feigl, 1998). Due to the extremely small rate of motion, geology is exceptionally difficult to be comprehended by humans and recorded by current technologies.

In the proximity of Patras, geological features on either side of the Patra-Rio fault zone are currently moving with few mm/year rate (Parcharidis et al., 2009a; Elias, 2013). Monitoring relative motion across faults in this urban-suburban area contributes to the assessment of seismic risks (Sitharam and Anbazhagan, 2007). In order to observe ground motion of mm/year, measurements on multiple locations should have taken place for at least a few years period (Strozzi et al., 2000). On-site permanent equipment exists, but not on nearly enough positions and most of it for merely adequate years. Luckily, systematic measurements for over 25 years, have been taken from space with the use of Earth-observing radar satellites.

The results of this dissertation can be used for risk assessment planning and better understanding of our environment. Moreover, since the data used are open and the equivalent data produced in the future by the Copernicus program are bound to be free, the observations can continue despite economical difficulties of the state.

2 Synthetic Aperture Radar basics and SAR interferometry

The radar sensors operate in the microwave band of the electromagnetic spectrum. Their wavelengths are 100 thousand times longer than those of the visible spectrum (Ferretti, 2014). Wavelengths that long can penetrate atmospheric media without significant signal loss. Furthermore, since Synthetic Aperture Radar (SAR) systems transmit and receive electromagnetic waves, they can provide all-weather and round-the-clock (nighttime included) images (Massonnet and Feigl, 1998).

Interferometric SAR (InSAR), is capable of measurements of the signal travel path because it is coherent (Ferretti et al., 2007a). InSAR characteristics make it ideal to monitor dynamic processes on the surface of the Earth (Moreira et al., 2013).

2.1 SAR system

A typical SAR imaging system from a satellite is sketched in Figure 1 . A satellite is equipped with a radar, the antenna pointed towards the Earth's surface, direction which is called Line Of Sight (LOS) or slant-range and is perpendicular to the orbit (Ferretti, 2014). The angle of the antenna with respect to the nadir of the satellite, is called the off-nadir angle (Ferretti et al., 2007a). The most known radar equipped satellites are right-looking in near-polar sun-synchronous orbits. This gives the opportunity to observe a particular location on the Earth on both ascending and descending orbit passes (Simons and Rosen, 2007). The two different look angles (ascending and descending) are the aftermath of both Earth rotation (E–W) and satellite near polar orbit for every satellite cycle (Ferretti et al., 2007b).

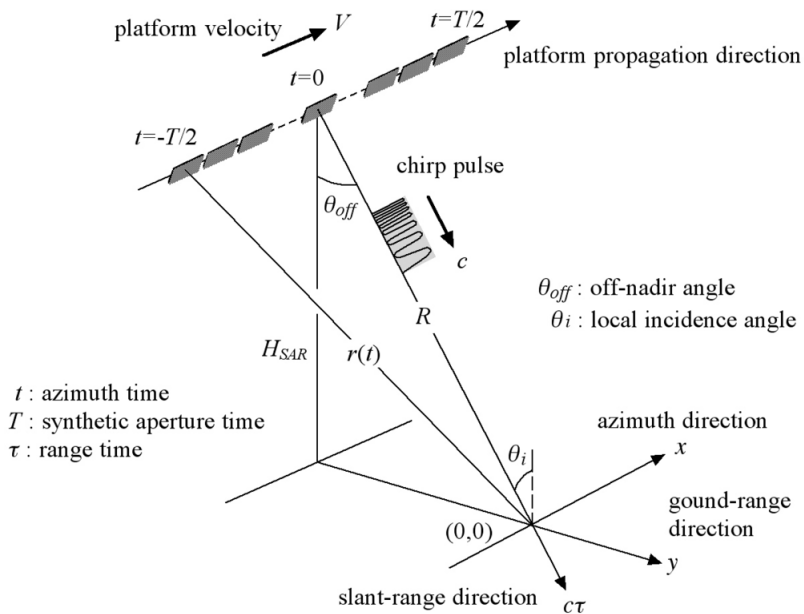


Figure 1: SAR systems' geometry and terms. H_{SAR} is the height of the SAR platform, c is the velocity of the microwave, and $r(t)$ and R are the slant-range distances at the azimuth time t and when the antenna is nearest to the target at the origin of the ground coordinate system (x, y) (Ouchi, 2013).

Satellite radar systems ordinarily transmit polarized radar pulses (Ferretti, 2014). The broadcasted microwave pulses are of alternating horizontal (H) and vertical (V) polarizations (Figure 2), and part of the horizontal and vertical components are backscattered and received (Ouchi, 2013). Thus, SAR data sets can be VV (Vertical transmit, Vertical received), HH, VH or HV (Ferretti, 2014). Better interferometric results are more luckily to occur while analyzing co-polarized data (i.e. HH, VV) due to the fact that co-polarized data have stronger signal, compared to cross polarized data (i.e. HV, VH) (Wessels, 2017a).

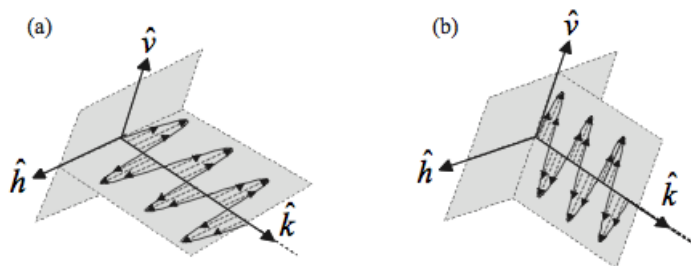


Figure 2: Polarimetric radar transmitted waves: (a) Horizontally (b) Vertically (Vasile and Besic, 2013).

2.2 SAR images

The SAR images are composed of the back-scattered portion of the initially transmitted electromagnetic pulse. The amplitude and phase of the back-scattered signal depends on the physical and electrical properties of the targeted object, as well as the frequency band used by the satellite (Moreira et al., 2013). Every pixel gives a complex number carrying amplitude and phase information about the back-scattered signal, from all the scatterers (rivers, crops, buildings etc.) within the corresponding resolution cell projected on the ground (Ferretti et al., 2007a).

The complex numbers of the acquired matrix can be interpreted as follows: amplitude values are related to local reflectivity of the back-scattered energy, while phase values are computed from local reflectivity and a quantity related to the distance between the target and the sensor (Ferretti et al., 2006). For those who are unfamiliar with the quantity related to target-sensor distance, an explanation will be attempted. As the sinusoidal wave travels in the air, the phase of the wave changes from 0 to 2π or every wavelength of distance traveled. SAR systems transmit a signals with known π value and can record the phase of the return signal very precisely (Osmanoglu et al., 2015). So, the distance between sensor and target can be expressed as an integer number of wavelengths, plus a segment equal to a fraction of the wavelength (Ferretti, 2014).

As SAR systems produce coherent images, several scatterers are present within each resolution cell and the 'speckle' effect is produced (Ferretti et al., 2007a). Also known as salt and pepper noise, 'speckle' cannot be found in optical images (Ferretti, 2014). The coherent sum of amplitudes and phases of scatterers per cell, fluctuate significantly from cell to cell (Moreira et al., 2013). Speckle noise reduction is achieved by averaging amplitude values (Ferretti, 2014)

2.3 SAR Interferometry

InSAR is the multiplying procedure of one SAR image to a second one, producing an interferogram (Hooper et al., 2012). The interferogram's amplitude is the multiplication of of the two images' amplitude, while the phase is the phase difference of the two images (Ferretti et al., 2007a). The two images analyzed must have been acquired from different vantage points, different times, or both (Simons and Rosen, 2007).

The measured phase difference, between two corresponding pixels, is

$$\Delta\phi = \phi_{topo} + \phi_{flat} + \phi_{disp} + \phi_{orbit} + \phi_{atm} + \phi_{noise} \quad (1)$$

where ϕ_{topo} is topography phase signature, ϕ_{flat} is flat earth phase caused by the imaging geometry, ϕ_{disp} is differential displacement pattern, ϕ_{orbit} is phase error caused by inaccurate orbit parameters, ϕ_{atm} is atmospheric artifacts and ϕ_{noise} refers to noise contribution (Elias, 2013).

The interferogram level's the Earth's surface, due to the geometry of SAR images and the slant-range imaging, thus objects of the same altitude have the same interferometric phase (Παρχαρίδης, 2015), producing what is called orbital fringes (Ouchi, 2013). A flattened interferogram can be computed by subtracting the expected phase from a surface of constant elevation (Simons and Rosen, 2007). As a result (Figure 3) often, phase cycles of 2π radians are seen, resembling to contour lines and the altitude between two 2π radians is called the altitude of ambiguity:

$$h_a = \frac{\lambda R \sin\theta}{2B_n} \quad (2)$$

where λ is the transmitted wavelength, R is the radar-target distance, θ is the radiation incidence angle with respect to the reference and B_n is the perpendicular baseline (the vertical component along the line of sight, of the distance between the two satellites) (Ferretti et al., 2007a).

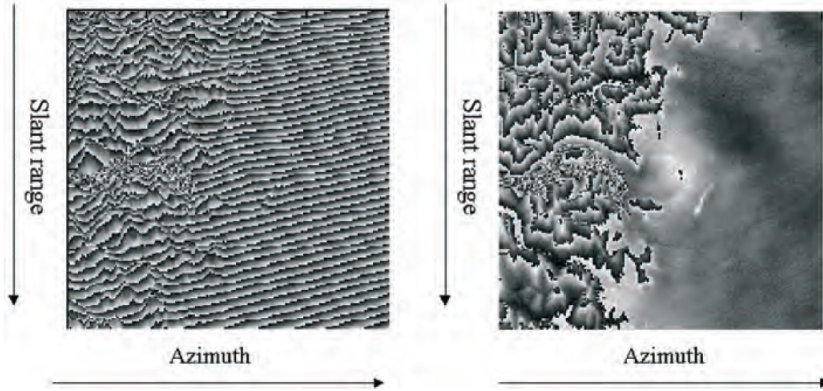


Figure 3: Unflattened (left) and flattened (right) interferogram of a portion of the Italian Alps and the Pianura Padana (Ferretti et al., 2007a).

2.3.1 Coherence of interferometric images

The degree of correlation -similarity- of the master and slave SAR images is expressed with signal-to-noise ratio (SNR), where similar images produce interferograms with high SNR (Moreira et al., 2013; Ferretti, 2014). Other than the important changes between the two SAR images, there are other parameters that can diminish the coherence: temporal, due to the change in the off-nadir angle, and due to random noise.

Temporal decorrelations $|\Delta r|$ describes changes in the scatterer characteristics between two time-separated SAR images (Moreira et al., 2013). In time, scatterers tend to become randomly rearranged, the detailed speckle patterns of the image resolution elements differ in each image acquisition, so the images are no longer correlated (Simons and Rosen, 2007). In order to minimise temporal decorrelation, the use of images with small time difference in acquisitions is recommended. Also, acquisitions that occur during or shortly after significant weather events such as rain or snow falls should not be used (Wessels, 2017b).

Spatial decorrelation $|b_{\perp}|$ derives from different imaging geometries between the time of image acquisitions (Zebker and Villasenor, 1992). Different imaging geometries occur when the perpendicular baseline is non-zero and thus a ground cell is captured from slightly different looking directions, leading to a shift in the image's spectra (Manunta, 2009; Elias, 2013). Spatial decorrelation makes impossible the interpretation of interferometric phases for extended targets in image pairs with baselines longer than the $|b_{\perp c}|$ critical baseline (Werner et al., 2003). Critical baselines differ per satellite and can be computed mathematically, as an example, for the ERS satellites the critical baseline is of about 1200m for a flat terrain, however the use of baselines greater than 600m are not recommended (Casu, 2009).

Complex correlation coefficient γ in pixel basis is measured as:

$$\gamma = \frac{E[u_1 u_2]}{\sqrt{E[|u_1|^2]} \sqrt{E[|u_2|^2]}} \quad (3)$$

where E is the expected value of the random variable x , and $|u_1|$, $|u_2|$ the amplitudes of the two initial images (Ferretti et al., 2007c).

From the complex correlation coefficient, the amplitude ranges from 0 to 1 and is known as coherence (Ferretti, 2014). Otherwise, phase independant coherence (Ferretti et al., 2007c) can be estimated

with the intensities (squared amplitudes) of the images (I_i):

$$|\hat{\gamma}|_q = \sqrt{\frac{\sum_i I_{1i} I_{2i}}{\sqrt{\sum_i I_{1i}^2} \sqrt{\sum_i I_{2i}^2}}} - 1 \quad (4)$$

Coherence value zero expresses the interferometric phase being just noise, while one defines complete absence of phase noise, meaning similar images (Ferretti et al., 2007a). In coherence maps, like the ones in Figure 4, bright areas show high coherence with values near to 1, while areas with coherence value near 0 have dark colours (Veci, 2016b).

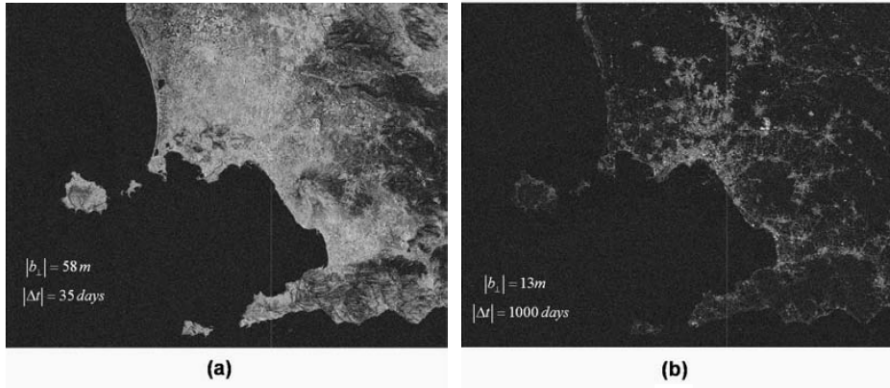


Figure 4: Coherence maps from ERS images: (a) refers to a small baseline and a small temporal separation, (b) refers to very small baseline separation and temporal decorrelation (Manunta, 2009).

2.3.2 SAR Differential Interferometry

Changes on the Earth's surface, can be measured along the line of sight of radar satellites using differential interferometry. Map elevation changes can be measured with differential interferometry (DInSAR) (Parcharidis et al., 2009a). DInSAR can recognize displacements of the Earth surface at a wavelength scale (Moreira et al., 2013). The principal theory is that interferogram is produced while the Earth's surface was stationary over time or the interferogram was produced instantly (Simons and Rosen, 2007). Once the terrain heights or digital elevation model (DEM) is removed, the interferogram is primarily composed of surface deformation and atmospheric disturbances (Klemm et al., 2010). After the DInSAR technique, the interferogram represents displacement of the surface between acquisitions, plus some other components (Hooper et al., 2012) which can be distinguished by their characteristics, like atmospheric effects being spatially correlated or noise phase which is uncorrelated (Ferretti, 2014).

If atmospheric effects and noise are neglected, and on top of that, flat Earth contribution has been dealt with, the DInSAR technique will produce an interferogram with fringes deriving from surface deformation phenomena (Ferretti, 2014). The interferometric fringes' wavelength or width is calculated as $\lambda/2$, half the radar wavelength (Ouchi, 2013). Hence, the accuracy of DInSAR is dependent from the SAR system used, approximately from 15 to 375mm, depending on the radar frequency (Rosen, 2011).

Assuming that the interferometric fringes serve as a full 2π cycle, each cycle being half the sensor's wavelength, proportionate ground movement between two points can be estimated by multiplying the fringes with half of the wavelength. Consequently, significant movement on the ground will be depicted with dense fringes, while no fringes will be produced if the two points-scatterers remained stable, with respect to one another, between the two image acquisitions (Veci, 2016b).

2.4 Phase unwrapping

InSAR phase measurements are wrapped between 0 and 2π , but more practical applications demand continuous phase values called unwrapped phase (Osmanoglu et al., 2015). Topography and motion of the surface can be estimated with absolute phases, whereas interferometric phase computed from the two images has values between $-\pi$ and $+\pi$ (Ferretti et al., 2007c).

Phase unwrapping (PU) is used to estimate the true phase profile of the wrapped interferogram, as in:

$$\phi_{i,j} = \psi_{i,j} + 2k\pi \quad (5)$$

i,j are the corresponding pixels of the two images, ϕ_{ij} is the unwrapped phase, ψ_{ij} is the wrapped phase and k is the positive or negative integer of 2π multiples (Abdelfattah, 2009) and shown in Figure 5.

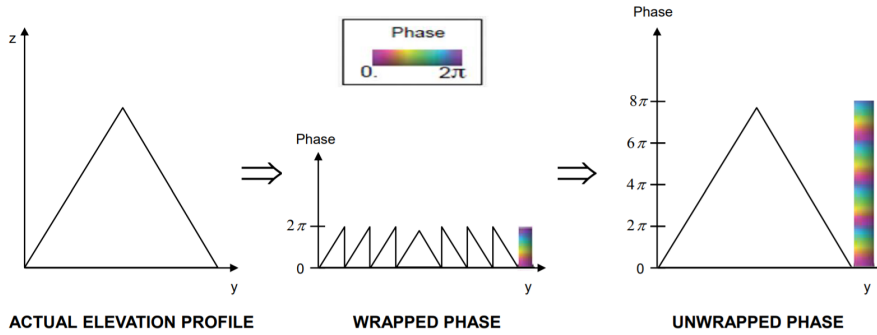


Figure 5: Modified illustration of wrapped and unwrapped phase from [Van-Zyl \(2017\)](#) and [Veci \(2016a\)](#).

However, pixels without important radar return may not give wrapped phases and even the given phases may originate from part of the topography which creates layover or foreshortening. So, when producing only one interferogram, the outcome of phase unwrapping may be questionable without any obvious answers, unless hypotheses are made on the structure of the underlying topography ([Ferretti et al., 2007c](#)). Nonetheless, in a multi-temporal DInSAR, use of temporal relations among considerable data of interferometric phases, can help the PU process ([Casu, 2009](#)).

2.5 Multi-temporal techniques

Multi-temporal radar acquisitions can be utilised to monitor surface deformation over time ([Tompolidi, 2017](#)). Extended SAR series images are able to detect and monitor deformations. Some past catastrophic events might have been more appropriately managed by using to multi-temporal InSAR, like the bridge collapse at Entre-os-Rios ([Sousa and Bastos, 2013](#)), however other tragedies have been prevented, like the road collapse on Elba Island which was detected and sufficient measures had been taken([Intrieri et al., 2015](#)).

2.5.1 Interferometric stacking

With this technique, multiple unwrapped differential interferograms are combined in order to estimate the linear rate of differential phase and visualize it on a single differential map ([DeZan and Lopez-Dekker, 2011](#)). The purpose of stacking separate interferograms is to reduce the noise ([Williams et al.,](#)

1998) and hence increase the signal to noise (S/N) ratio (Manconi, 2017).

A simple stacking technique to produce a mean image is:

$$S_{i,j} = \text{mean}[I_1(i, j), I_2(i, j), \dots, I_n(i, j)] \quad (6)$$

where n is the number of interferometric images, $i=1, \dots, K$ and $j=1, \dots, L$, where K and L express the size of the images in pixels, and $I_m(i, j)$ is the pixel value at pixel location (i, j) (Elias et al., 2006).

Interferometric stacking enables a first estimation of the deformation pattern, recognition of relatively stable areas (Parcharidis et al., 2009a).

2.5.2 Persistent Scatterer Interferometry

The term Persistent Scatterer Interferometry (PSI) refers to all multi-interferogram techniques aiming at extraction of information from discrete scatterers (Ferretti, 2014; Raucoules et al., 2007). PSI enables the user to detect displacements of anthropogenic or natural reflectors, along the slant-range, by separating in time surface motions, atmospheric contributions, and digital elevation model error components of the range change measurement (Amato et al., 2017). Each approach has its differences, particular target behavior gave rise to various algorithms to solve for surface deformation (Osmanoglu et al., 2015).

Permanent Scatterer InSAR (PSInSARTM) is a technique capable to identify image pixels called permanent scatterers. Pinpoint of permanent scatterers (PSs), even smaller than the resolution cell, is feasible because they appear coherent over long time intervals regardless of the baseline (Ferretti et al., 2001).

The PSInSARTM technique was the first to find a solution to select PSs, overcoming the temporal and the geometrical decorrelation, estimating deformation and residual topographic error (Crosetto et al., 2016). PSs are usually man-made structures, making this technique exceptional for applications in urban environments (Ferretti et al., 2006). When referring to urban environments, the PSs are usually roofs reflecting energy directly backwards or, following a double-bounce, structures where energy is reflected firstly from the ground and secondly from structure (Hooper et al., 2012). PSs are dense in

urban areas (up to 1000 PS/km² with ERS and Envisat data), though sparse in vegetated and forested areas, where smooth surfaces and steep terrain is more common (Crosetto et al., 2009).

Interferometric Point Target Analysis (IPTA) shares the same basic theory with PSInSARTM (Osmanoglu et al., 2015). They both apply on full resolution data (single look data) and rely on the measurement of deformation on a spatial grid of amplitude PSs candidates (Casu, 2009). IPTA makes use of the temporal and spatial characteristics of interferometric signatures collected from potential PSs to accurately map surface deformation phenomenons, terrain heights, and relative atmospheric path delays (GAMMA, 2013).

In the interferometric point target analysis the interferogram is only interpreted for the selected points, using vector format data structures. In brief, IPTA makes constant improvement of the model parameters to obtain an optimal match to the detected interferometric phases for a selected list of PS candidates. In Figure 6, a typical flowchart of IPTA processing sequence is illustrated (Werner et al., 2003).

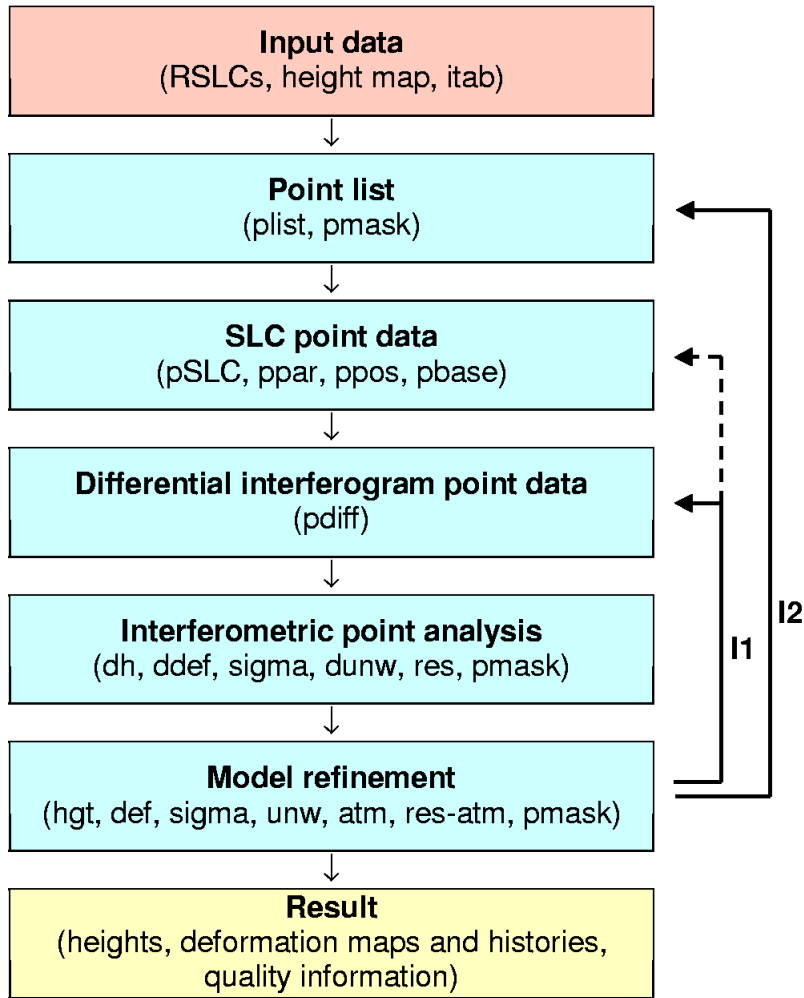


Figure 6: Interferometric point target analysis (IPTA) processing graph (Werner et al., 2003).

2.5.3 Small Baseline Subset

The Small Baseline Subset (SBAS) technique is based on the use of an abundant number of SAR images distributed in small baseline subsets, granting an easy combination of DIFSAR interferograms and computation of mean deformation velocity maps and time series (Lanari et al., 2007). A SBAS technique diminishes the separation in both baseline and Doppler frequency of SAR pairs, thus maximizes the interferogram correlation (Qu et al., 2015).

On a $N + 1$ SAR images, acquired for the same area and chronologically from t_0, \dots, t_N , M possible interferograms will be computed, but every small baseline subset is composed by a minimum of two acquisitions. These interferograms should have their phase signal unwrapped and calibrated based

to one pixel whose deformation is known. What is more, the SBAS technique is applied on pixel by pixel basis where coherence is sufficiently high. From the interferograms computed, the deformation of each pixel organized in a matrix representation:

$$A\phi = \delta\phi \quad (7)$$

where A is the $M \times N$ matrix, so that $\forall_j = 1, \dots, M$ and $A(j, slave_j) = -1$ if $IS_j \neq 0$, $A(j, master_j) = +1$ and zero otherwise. Lets say that $\delta\phi = \phi_4 - \phi_2$ and $\delta\phi = \phi_3 - \phi_0$, then it would be illustrated as:

$$A = \begin{bmatrix} 0 & -1 & 0 & +1 & \dots \\ 0 & 0 & +1 & 0 & \dots \\ \dots & \dots & \dots & \dots & \dots \\ \dots & \dots & \dots & \dots & \dots \end{bmatrix} \quad (8)$$

So, the SBAS method makes use of all the acquisitions in the various small baseline subsets and provides spatially dense deformation maps. Additionally, the utilization of time and space information allows the removal of a considerable amount of atmospheric artifacts via a proper space–time filtering operation ([Berardino et al., 2002](#)).

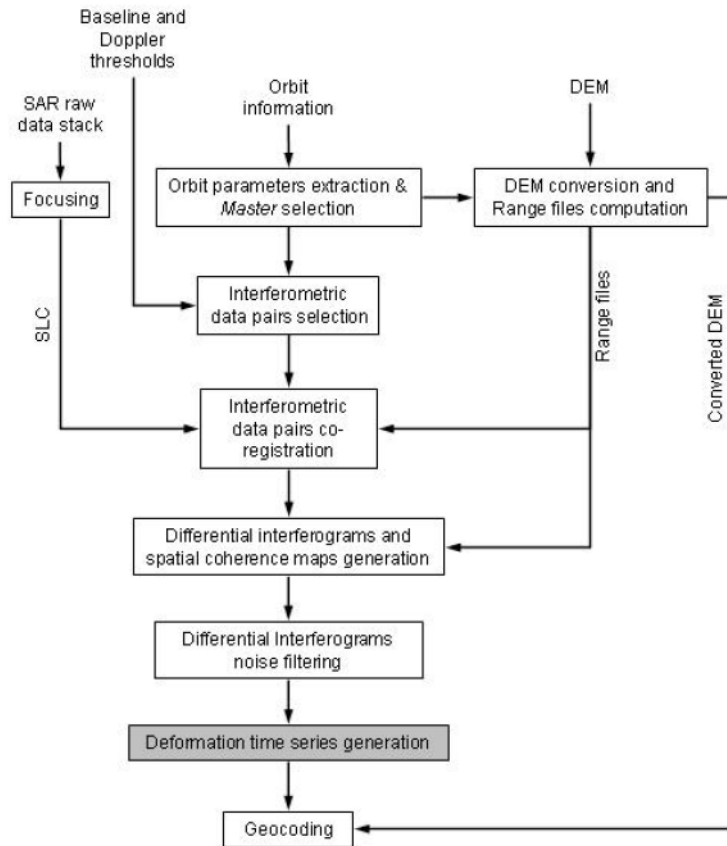


Figure 7: Small Baseline Subset (SBAS) processing graph (Casu, 2009).

2.5.4 Hybrid method with SVD

Methodologies of “hybrid InSAR” adopt characteristics of conventional DInSAR, short baseline interferometry and PSI approaches. Using elements of different interferometric analysis, difficulties of each approach can be overcome.

Since A in equation (8) has a rank deficiency in case of multiple small baselines subsets, the Singular Value Decomposition (SVD) can be used to “link” separate SAR datasets. The SVD technique will decompose A into its pseudoinverse matrix and the minimum-norm LS solution of the system will be easily computed, for more information refer to (Berardino et al., 2002; Manunta, 2009; Benekos et al., 2014). SVD can be referred to as an interferometric post-processing step, the “natural extension” of a Least Squares (LS) problem. In LS, independent data sets are connected with the assumption of a linear trend of deformations within the time interval (Usai, 2003).

3 Geology

Generally speaking geology is the study of Earth: of its materials, of the processes that formed those materials, the water beneath or underneath the surface, the changes in the interior or the exterior of the Earth over the vastness of time, and the changes that are yet to come in the distant or near future (Earle, 2015).

Geology has been divided to several branches, from which this thesis is more related to physical geology. Physical geology studies the physical forces and processes which shift Earth's crust and/or surface (Jain, 2014). The purpose of physical geology is to understand Earth's process that form our environment, the genesis and location of earth materials and Earth's hazards (Duff, 1993).

3.1 North-Western Peloponnese

3.1.1 Stratigraphy

In the studied area two geotectonic units can be seen (Figure 8), the Gavrovo-Pilos unit from the continental tectono-stratigraphic terrane H1 and the Pindos unit from oceanic terrane H2 of the Hellenides (Papanikolaou, 2009).

Gavrovo-Pilos unit is consisted of limestone and flysch. This unit is can be found in the western part of the prefecture of Achaian (Νόρδα, 2015). Within the flysch marly clays, fine-grained sandstones, cohesive sandstones or even conglomerate horizons have been identified (Papanikolaou and Lekkas, 2008).

Pindos unit in the eastern area of the city of Patras, was well defined from early on. The unit is consisted of flysch, thinly-bedded limestones, their transitional beds and schist-sandstone-chert formations (Rozos et al., 2006).

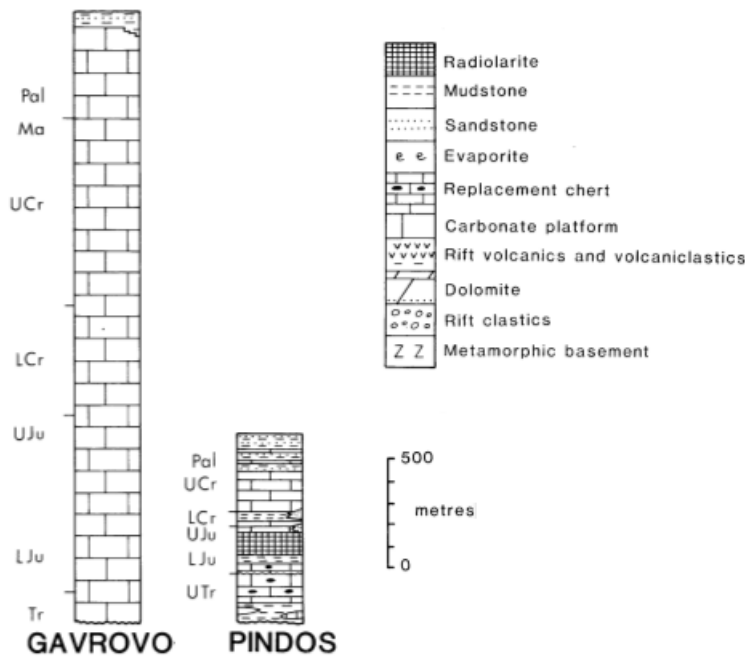


Figure 8: Stratigraphic columns, modified from (Robertson and Shallo, 2000).

However, these geological units have been covered by pliocene, pleistocene sediments and quaternary alluvial deposits (Pόζος, 1989). Acquired borehole data from the city of Patras have shown that the total thickness of the Plio–Pleistocene sequence exceeds 300 m (Koukis et al., 2005). As can be seen from Figure 9 the area is covered with:

clastic sedimentary rock: Sedimentary rock in which at least 50 percent of the constituent particles were derived from erosion, weathering, or mass-wasting of preexisting earth materials, and transported to the place of deposition by mechanical agents such as water, wind, ice and gravity.

diamicton: Unsorted or poorly sorted, clastic sediment with a wide range of particle sizes, including a muddy matrix. Biogenic materials that have such texture are excluded. Distinguished from conglomerate, sandstone, mudstone based on polymodality and lack of structures related to transport and deposition of sediment by moving air or water. Assignment to an other size class can be used in conjunction to indicate the dominant grain size.

biogenic silica sedimentary rock: Sedimentary rock that consists of at least 50 percent silicate mineral material, deposited directly by biological processes at the depositional surface, or in particles formed by biological processes within the basin of deposition.

gravel: Clastic sediment containing greater than 30 percent gravel-size particles (greater than 2.0 mm diameter). Gravel in which more than half of the particles are of epiclastic origin.

limestone: Pure carbonate sedimentary rock with a calcite (plus aragonite) to dolomite ratio greater than 1 to 1. Includes limestone and dolomitic limestone.

sandstone: Clastic sedimentary rock in which less than 30 percent of particles are greater than 2 mm in diameter (gravel) and the sand to mud ratio is at least 1.

clastic sediment: Sediment in which at least 50 percent of the constituent particles were derived from erosion, weathering, or mass-wasting of preexisting earth materials, and transported to the place of deposition by mechanical agents such as water, wind, ice and gravity (INSPIRE, 2012).

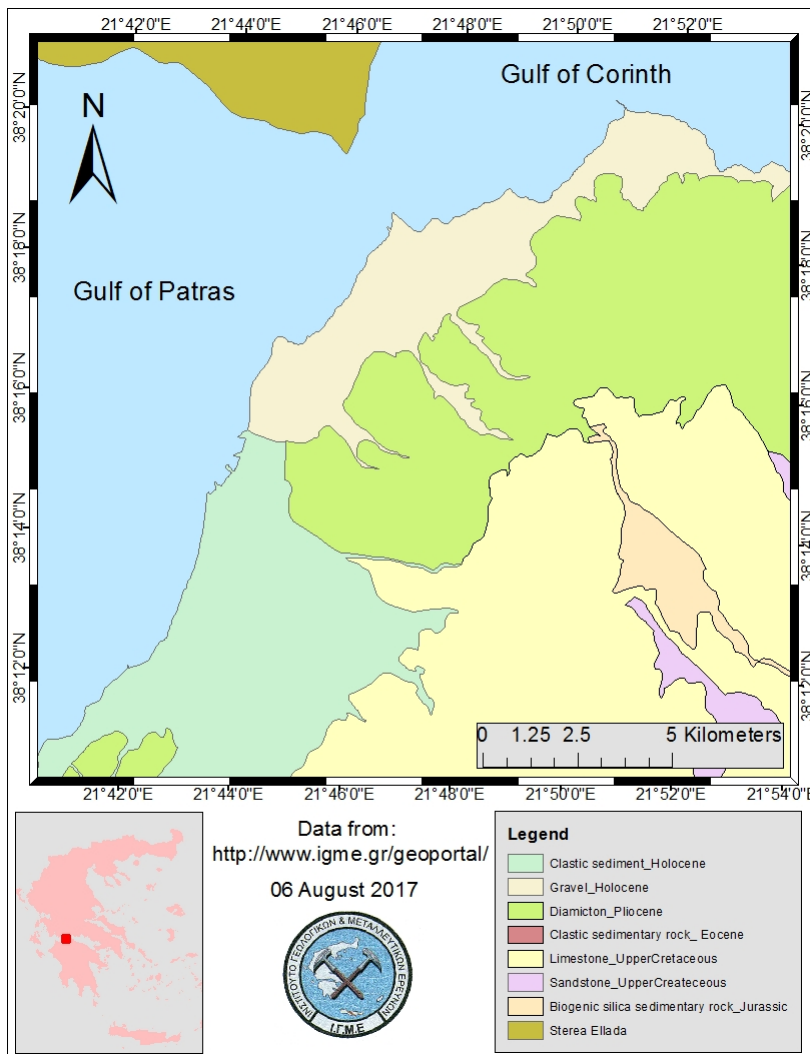


Figure 9: General geologic map with data from the (I.G.M.E., 2017).

3.1.2 Geo-dynamics

The eastern Mediterranean, as seen in Figure 10, is considered to be tectonically active at the present time with apparent complexity of the geology and the interaction of tectonic effects (Woodside, 1977). The Mediterranean Ridge can be seen as a young submerged chain associated with continent-continent compression acting along the Hellenic Arc, basically formed by thrust belts (Calvagnile et al., 1982).

The tectonic framework of the area is dominated by the the relative north-northwest and northward motion of the Arabian and African plates respectively, colliding with Eurasia. The leading edge of the African plate is being subducted along the Hellenic arc at a higher rate than the relative northward motion of the African plate itself, requiring that the arc (and presumably the Aegean Sea) moves southward relative to the Eurasian plate (Oral et al., 1995). North Aegean is a region which links pure strike-slip faulting of North Anatolian Fault (NAF) and pure extension in central Greece (McNeill et al., 2004).

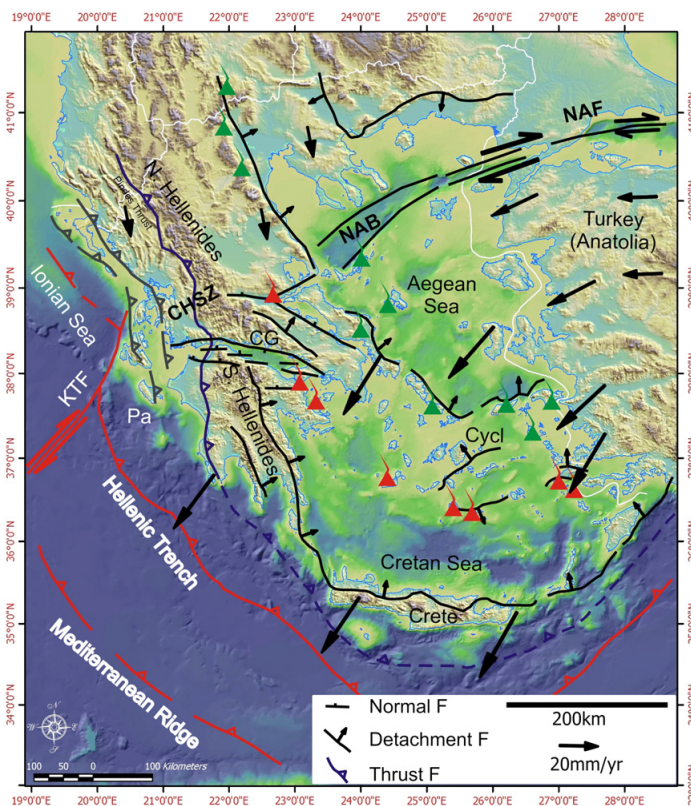


Figure 10: Simplified geological map of the Rio-Antirio broader area (Parcharidis et al., 2009a).

3.1.3 Neotectonics

The extension occurring in Western Greece from Pliocene till today, is an aftermath of the southern movement of the Aegean Sea, giving birth to the Corinth rift (Θεοδωρακόπουλος, 2015). Throughout the Mediterranean region, the Corinth rift zone has been acknowledged as one of the most rapidly developed inter-continental rifts (Koukis et al., 2005). The Corinth rift is consisted of three grabens: the Corinth graben, the Rio graben and the Patras graben (Figure 11). From those, the first to occur where the Rio graben and an eastern part of the Corinth graben which expanded towards the Rio graben. Also, the Patras graben has the most recent sediments (Τσόδουλος, 2009).

The Western Corinth graben is characterised by WNW normal faults, caused by the southern Aegean motion, and NNE transfer faults due to the expansion and the uplifting of the area. The WNW normal faults have a NNE direction, they are up to 40 km long, they are syn-sedimentary, between 60 and 80 degrees, maximum vertical throw has been measured as 800m and have a slip rate of 0.11 to 0.44 mm/yr. The NNE transfer faults have mostly a ESE direction, they are up to 11 km long, they can cause slopes of 20 to 50 degrees, the transfer zones can be classified as divergent or convergent, relay ramps can be observed, maximum vertical throw has been measured as 450m and have a slip rate of 0.08 to 0.14 mm/y (Πόζος, 1989).

The Rio graben terminates in the west at the Patras graben zone, while it is connected in the east with the Corinth graben. Whereas this graben shows low seismicity, an important number of seismic events takes place in the region of Naftaktos (where Rio and Corinth graben connect). Major structural trends in this area vary between NE and ENE and are cut by high-angle normal faults which dip to the NNW. Additionally, WNW faults are older but active, and with the ENE faults, they trend to change to E-W like the curved and anastomosing fault scarps north and south of the University campus (Doutsos et al., 1988).

The Patras graben is a 40-km long fault zone from cape Araxos to the Ellinikon village. Blocks are made by widely spaced WNW trending normal faults. NNE transfer faults have occurred due to depositional changes in downthrown blocks (Parcharidis et al., 2009b). Quaternary vertical slip on the central parts of Patras basin is about 3–5 mm/yr. The Patras graben today represents the early stage of the Corinth graben (Doutsos et al., 1988).

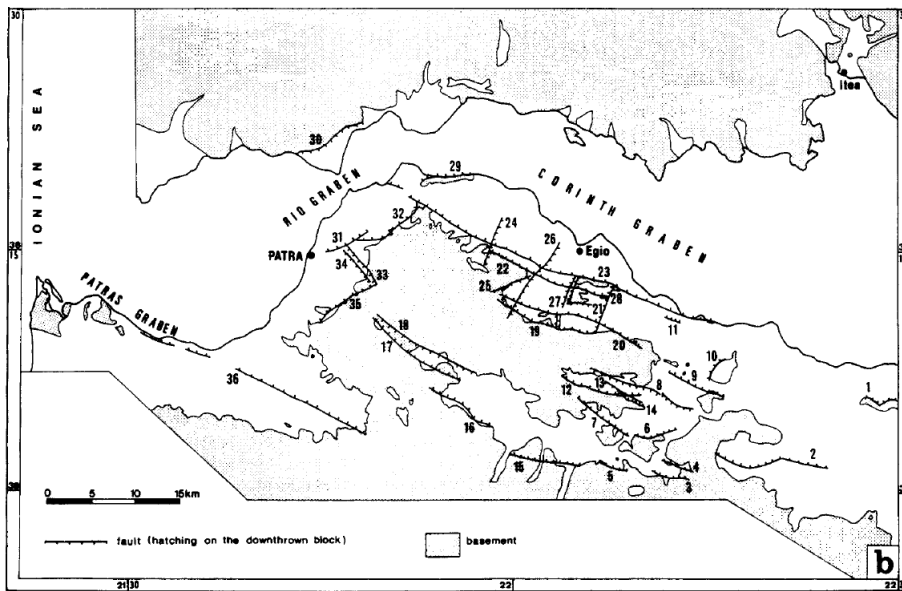


Figure 11: Tectonic map of the primary active faults (Doutsos and Poulimenos, 1992).

3.1.4 Seismicity

Many researchers have identified the eastern Mediterranean as an ideal natural laboratory for studying the kinematics and dynamics of plate interactions, because its seismicity categorises it as one of the most tectonically active regions on Earth (Plag et al., 1998; Rontogianni, 2010; Ford et al., 2013). As the automation and new correction techniques have enabled more reliable motion recordings (Margaris et al., 2002), it has been appointed that, Greece astonishingly releases about 2% of the whole world's seismic energy, which corresponds to more than 50% of Europe's seismic energy (Koukis et al., 2005).

Within Greece, the city of Patras in NW Peloponnese is surrounded by some of the most seismically active seismogenic structures (tectonic faults and grabens of recent geodynamic evolution) (Koukis et al., 2005; Mantyniemi et al., 2004). Although the seismic activity was continuous since the ancient times, the combination of historical data and geomorphological observations is fundamental to determine and date the reactivation of faults (Gaki-Papanastasiou et al., 1996). Afterwards, those faults can be registered in an earthquake catalog, necessary for seismic hazard, seismic risk, seismic zonation evaluation as well as for future planning of land use (Burton et al., 2004).

From earthquake catalogs, maps can be produced such as the one of Figure 12. Regarding historical data about Greece, philosophers in greek and latin language have started writing down seismic events

after 6th century B.C.. Up to 1000 A.D., ancient and Byzantine texts account the most significant earthquakes. From 1000 to 1500 A.D. Byzantine historians mark down most of the seismic events, and the others can be found in archives, chronicles and marginal notes. Until 1900, historical earthquakes are reported in Ottoman archives, diplomatic archives, monastery books and other sources (Kouskouna and Makropoulos, 2004). By 1911, the first seismometer (Mainka with 2 horizontal components) was installed in Athens, defining the end of Greek historical earthquake data (Kouskouna and Makropoulos, 2004; Lee et al., 2003).

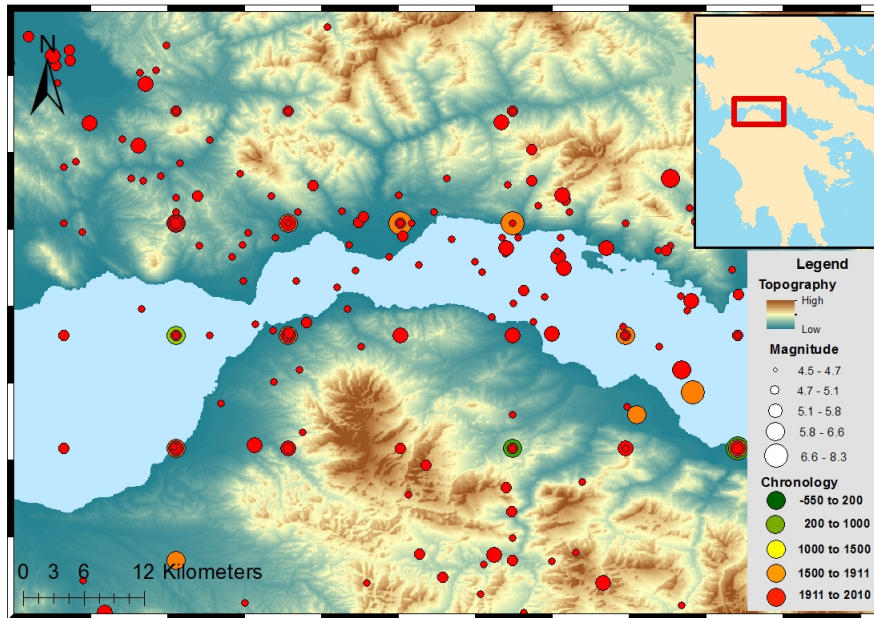


Figure 12: Seismicity map of broader area of Patras, from 550 B.C to 2010. Complete data are illustrated only for the following periods and magnitudes $M > 6.5$ since 1901, $M > 5.2$ since 1911, $M > 4.8$ since 1950 and $M > 4.5$ since 1964, data from A.U.TH. (1981), processed by the author.

More recent research has focused on the seismicity pattern of the area revealing that most of the events are shallow, occurring in depth of 2-25 km (Melis et al., 1989). Underneath Patras and western Corinth, shallow earthquakes take place due to the crustal extension (Kassaras et al., 2016). As the faults are active, giving frequently seismic events of small magnitude, permanent and non permanent networks of Global Navigation Satellite System (GNSS) monitor the area and can be accessed from sites like the CRL Near Fault Observatory portal or Noanet.

3.2 Surface motion

Earth's surface can be in motion due to one or multiple causes.

3.2.1 Subsidence

The ground surface mostly shifts downwards, for as many natural reasons as man made. Some of the reasons for a subsiding region are:

faults: The hanging wall of a normal fault or the footwall of a thrust fault are subsiding. Big blocks show displacement due to extension or compression of an area ([Molnar, 2015](#)).

compaction: Some lithologies are porous and contain fluid within them. If more sediments accumulate above these lithologies or buildings are constructed, the stress augments leading to liquid escape and porosity declination ([Doornhof et al., 2006](#)).

water pumping: Extended land subsidence can be caused by water pumping in unconsolidated aquifer systems ([Holzer, 1983](#)) and uplift can occur after the elastic rebound of the recharged aquifer ([Chen et al., 2007](#)).

extraction of ground resources: Subsidence can occur due to voids from mining underground salt, sulfur and other minerals or gas ([Lee and Abel Jr., 1983](#)) and in the long term uplift due to flooding ([Vervoort and Declercq, 2018](#)).

3.2.2 Elevation

Tectonic uplift occurs on the footwall of a thrust fault or the hanging wall of a reverse fault. Common places with significant elevation rates are zones of continental plates collision and the island arcs of oceanic plate subduction ([Cordonnier et al., 2016](#)).

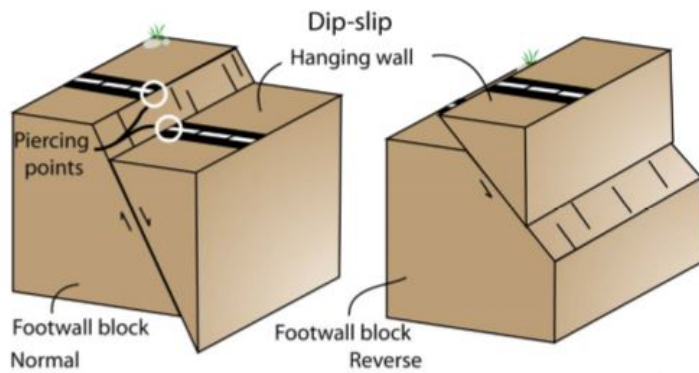


Figure 13: Diagrams of dip-slip normal and reverse/thrust faults (Girty, 2009).

3.2.3 Strike-slip faults

On strike-slip faults, the motion on the fault plane is horizontal and not vertical as apposed to subsidence or elevation. Some of the reasons for strike-slips faults to occur are: the separation of blocks moving because of plate convergence, the accommodation of different rates of displacements over a region, the transfer of horizontal slip between neighboring/almost parallel faults or the distinction of contrasting tectonic styles (Sylvester, 1988).

Tectonic ground motion is complex, with almost every time vertical and horizontal components. However, the faults are called oblique only when dip-slip and strike-slip components co-exist, are perceptible and measurable (IRIS, 2017).

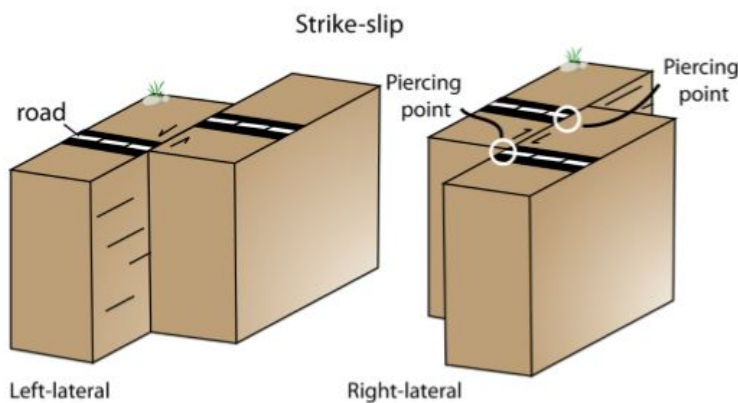


Figure 14: Diagrams of strike-slip faults (Girty, 2009).

4 Seismic Risk

A generic definition of seismic risk could be set as the probability of occurrence of the adverse consequences to society (Wang, 2008). In other words, seismic risk can be expressed as the probability that humans will expose themselves to loss or damage to their built environment if they are exposed to a seismic hazard (Wang, 2009b). A simple expression of seismic risk is the synergy of seismic hazard and vulnerability of humans or their built environment:

$$R = H * V \quad (9)$$

where R is the risk of the exposed population or potential damage to buildings, H is the factor of seismic hazard and V is the population or building vulnerability. Hence, high seismic hazard does not mean high seismic risk if exposure is low enough, and vice versa (Sipos and Hadzima-Nyarko, 2017; Wang, 2009a).

Even though seismic risk is proportional to seismic hazard, cities with dense population tend to have the higher earthquake risk (Papadopoulos and Arvanitides, 1996). Patras in particular, being the third largest city of Greece, had an urban planning where geological setting and processes were not taken accurately into consideration, leading to higher seismic risk (Koukis et al., 2005; Tselentis et al., 2004).

4.1 Seismic Hazard

Seismic hazard is often confused with seismic risk and given the same definition as in (Cornell, 1968), so it is important to clarify their meaning. Hazard can be any natural or man-made phenomenon, capable to harm society (Panza et al., 2011). Earthquake or seismic hazard is the likelihood of ground motions (or another parameter) to exceed a given value over a specified time period (Gupta, 2007; Tsipianitis, 2015).

With the use of the whole seismological record, taking into account both historical and instrumental data, and without using any specification of seismic sources or/and seismic zones, the seismic hazard can be mapped practicing a probabilistic approach (Tsapanos et al., 2004). For engineering

applications, a commonly considered parameter for seismic hazard is peak ground acceleration (PGA) (Solomos et al., 2008). As seen in Figure 15, the studied area of Patras-Rio has a high value of PGA.

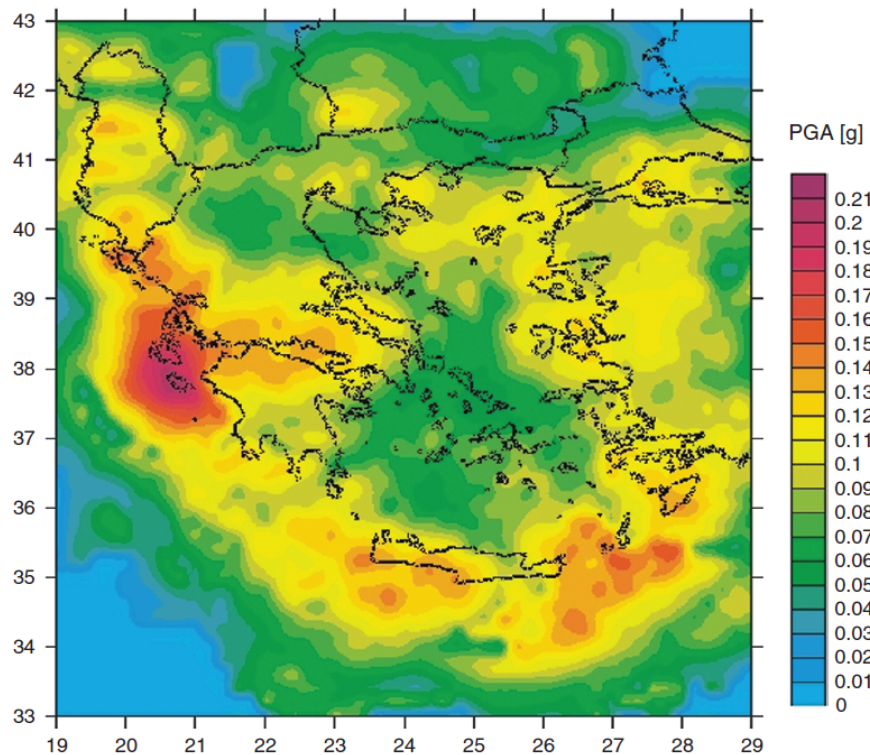


Figure 15: Smoothed probabilistic seismic hazard map of Greece and adjacent areas in terms of PGA values at 10% probability of exceedance, until 2054 (Tsapanos, 2008).

4.2 Vulnerability

The vulnerability of the area to earthquakes is related to the physical condition of the built environment, the exposure of the city, and lastly, social and economic conditions (Tselentis et al., 2004).

Seismic vulnerability to buildings is depended on seismic deficiency of that building, meaning the conditions that deteriorate the building's performances (El-Betar, 2016). During an earthquake, the structural members of the buildings should be capable to preserve a certain amount of integrity (M. Mucciarelli et al., 2001). Some of the parameters taken into consideration for vulnerability assessment are: the age of the structure, the building's height, the visible ground settlement, distance between seismic zones and the city, etc. (Alam et al., 2012).

When evaluating seismic risk, the exposure refers to the assets or population that are at risk such as buildings, transportation lines or population's density (Wieland et al., 2012). Also, population exposure varies significantly in temporal cycle, like night and day (home and place of work) or mid-summer and autumn (vacation travels) (Freire and Aubrecht, 2012).

The social and economical status plays a vital role in vulnerability, as it can be interpreted as resources for an efficient defense (Yucel and Arun, 2012). Social vulnerability to an earthquakes refers to the capability of a human community to resist, cope with, and recover from the impact of that natural hazard (Armas, 2008). Parameters within the social vulnerability are the: gender, age, social status, ethnicity, type of housing etc (Armas and Gavris, 2016). Finally, vulnerability is related to the economic loss expressed as mean damage ratio to the hazard's severity (Yamin et al., 2017).

The studied area is characterised by high vulnerability due to the large population, the large economic value of the exposed structures (Mantyniemi et al., 2004) and the active faults zones in the vicinity of the urban areas (Θεοδοσίου, 2015). Figure 16, illustrates some of the most active faults in the proximity of the urban and sub-urban studied area. In particular, Agia Triada fault zone (ATFZ) seems to be in the heart of Patras city and Patra-Rio fault zone (PRFZ) appears along a sub-urban area extending from Patras to Rio.

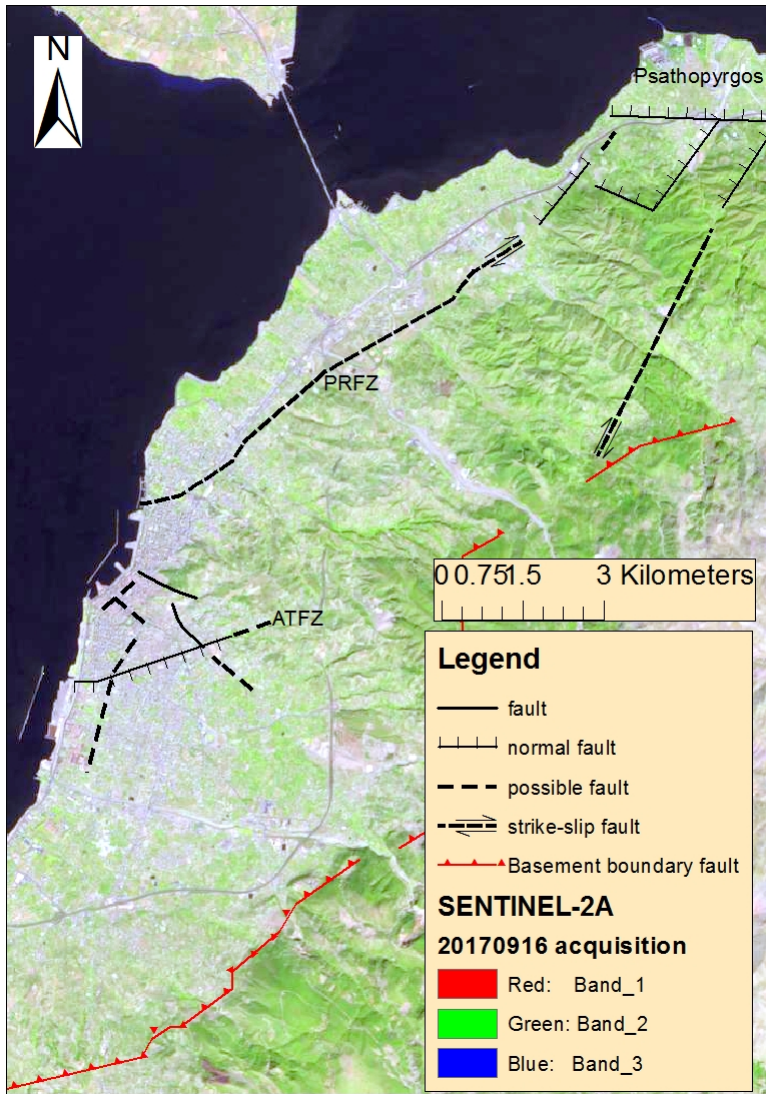


Figure 16: The faults demonstrated on a level-1C Sentinel-2A image, accessible from (USGS, 2017), are after the works of Flotte et al. (2005) and Koukis et al. (2005).

5 Literature Review

Almost eight years ago, [Parcharidis et al. \(2009a\)](#) studied the ground deformation over Rio-Antirio for the period 1992-2000 by means of InSAR techniques. In this case the PSs were mainly in and in near proximity of the urban areas. Near Rio, the points showed subsidence with almost linear ground deformation from -1.8mm/year to -6.2mm/year. Surroundings with higher altitude showed stability or even uplift from +2mm/year to +6mm/year. Towards Patras and East of Rio, subsidence rates decreased with no less than -1.5mm/year. The displacements in Rio were interpreted by the presence of the Rio-Patras transfer-fault zone.

The same year, [Parcharidis et al. \(2009b\)](#) investigated active faults in the cities of Patras and Pyrgos, applying a PS interferometric analysis on data between 1992 and 2000. The hanging wall of Rio-Patras fault showed subsidence of -4.5 to -5.5mm/year, however the footwall block revealed uplift velocities of +4.0 mm/year to +5.5 mm/year. The downthrown block of Agia Triada fault (ATf) was subsidising with rates of -1.0 to -2.8mm/year, while the footwall was uplifting with rates of +0.4 to +1.0 mm/yr.

Little less than 5 years ago, [Elias \(2013\)](#) observed ground deformation, occurring between 2002 and 2012, in the western Corinth rift using SAR interferometry. For the city of Patras, some discontinuities were common and the deformation seemed to be persistent for from 1992 to 2010 (Figure 17). The ground motion across the Rio-Patras fault zone (RPfz) was measured from 0.5 to 4mm/year. Moreover, Psathopyrgos Delta shown sediment compaction, and movement on the Psathopyrgos fault (Fig. 18).

With a few months time interval from Elias's PhD, [Sakkas et al. \(2013\)](#) made a combined study of ground deformations at the broader area of gulf of Patras. Through this study, GPS measurements for the period 1994-2006 combined with knowledge on the tectonic evolution, indicated regional uplifting with rate of approximately 8-10mm/year. Moreover, subsidence up to 5mm/year was identified in the coastal areas of Patras, correlated with Quaternary deposits, human activity and the downthrown side of RPfz.

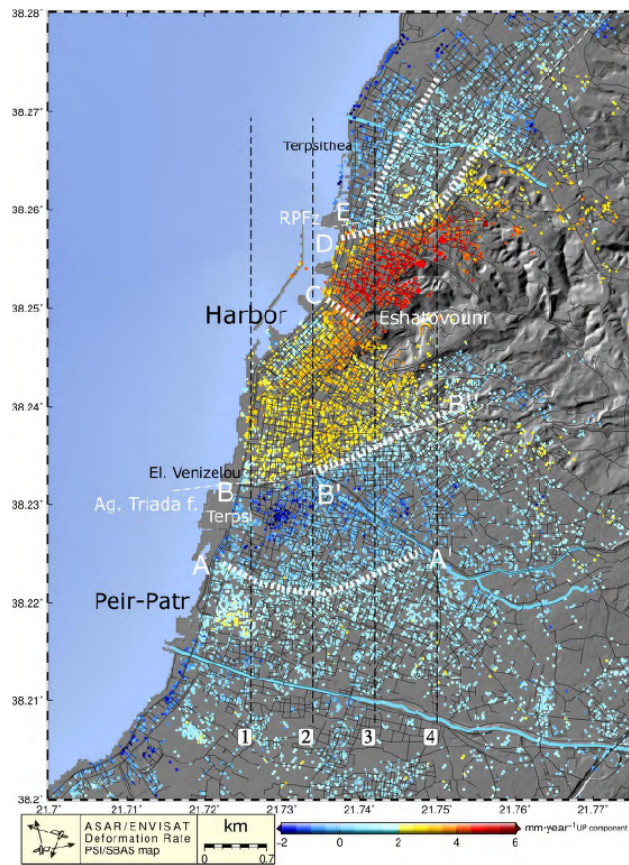


Figure 17: Map of the vertical rate of the city of Patras, using PSI/SBAS technique. The black dotted lines correspond to cross sections of original author. The main discontinuities of A-A', B until B' and to B'', at C, D, E until F ac be discriminated. The thin white dotted lines visualise the fault traces of Agia Triada and Rion-Patras fault zone (Elias, 2013).

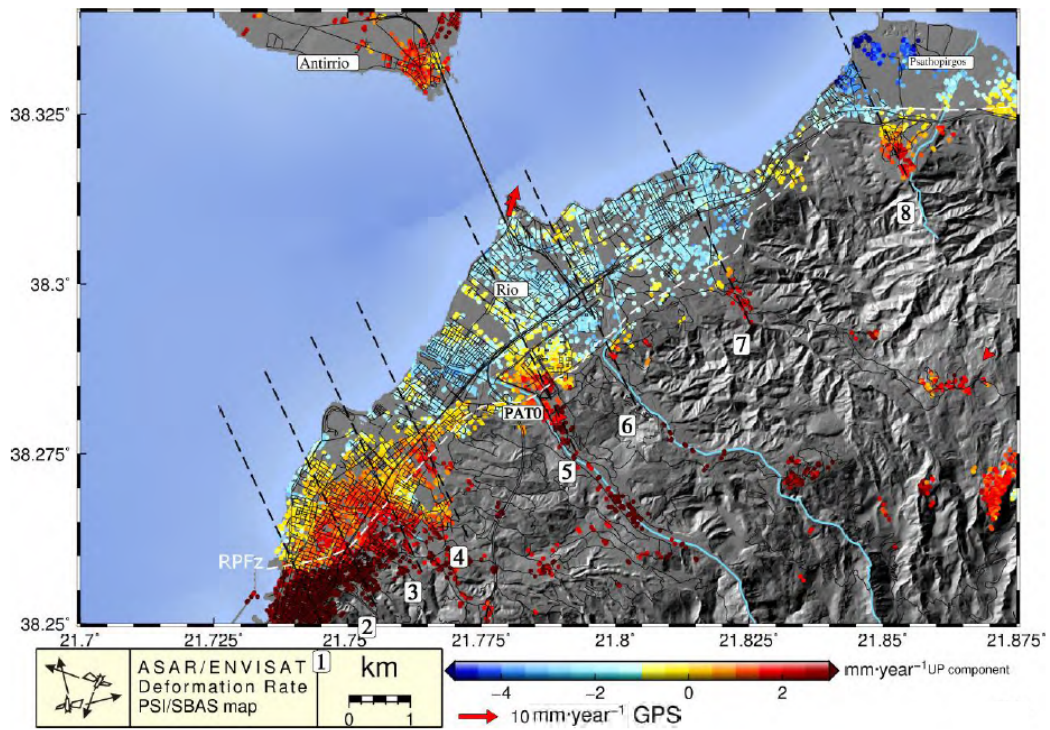


Figure 18: Map of the vertical rate of the Rion-Patras fault zone, using PSI/SBAS technique. The black dotted lines correspond to cross sections of original author. The white dashed line visualises the RPFz (Elias, 2013).

6 Data

6.1 Digital Elevation Model

The processing of SAR images has been done with a Digital Elevation Model (DEM) of 5m x 5m cell size, produced by the Hellinc Cadastre with aerial photogrammetry for their own needs. The original DEM was on traverse Mercator projection of GGCS87 Datum, but has been turned to Universal Transverse Mercator (UTM) projection and the corresponding DEM parameter file was computed with the GAMMA software.

6.2 Synthetic Aperture Radar Observation data

In this study Level 1 Single Look Complex (SLC) and Single Look Slant range Complex (SSC, here by referred to as SLC as well) image products were used from the satellites illustrated in Figure 19. SLC images are digital, amplitude and phase are encoded as complex numbers. The image's data are focused SAR data, geo-referenced and provided in slant-range geometry. Before being distributed the data had a minimum number of corrections and interpolations ([ESA, 2017a](#)).

For all of the processing, since the main area studied is urban and sub-urban, co-polarimetric (VV or HH) data has been used. This type of polarization provides strong signal due to double bounce effect on the buildings. Applying the same polarization over the time-series, the data can be more easily compared.

Satellite data has been provided by various sources. In order to access the ERS's and ENVISAT's catalogue of ESA's Earth Observation data products, the interactive multi-platform [Earth Observation Link - Stand Alone](#) (EOLi-SA) tool was used. TerraSAR-X imagery has been provided by DLR, in support of the Group of Earth Observations ([GEO](#)) [Supersite](#), using the EOWEB system. For Sentinel-1, [Copernicus](#) Sentinel data has been retrieved from [ASF DAAC](#).

Precise orbit state vectors have been additionally downloaded in order to estimate the interferometric baselines of the two older satellites. For Envisat, DORIS Precise Orbit State Vectors were generated by the Centre de Traitement Doris Poseidon (CTDP). For ERS, Delft Institute for Earth-oriented Space Research (DEOS) provided the study with highly precise orbits.

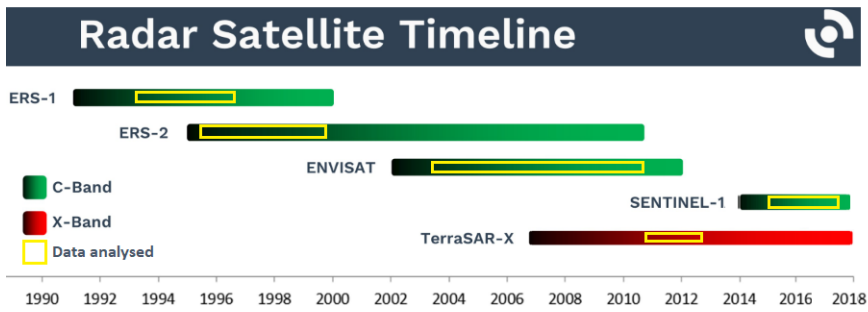


Figure 19: Here are illustrated the used satellites’ lifetime and type of band, configured from the original image [Schmullius \(2017\)](#).

6.2.1 ERS

ERS-1 and ERS-2 were European Remote Sensing satellites, launched for the scientific study of Earth’s environment. They both had a Sun-synchronous polar orbit, with ERS-1 being launched in July 1991 and ERS-2 in April 1995 ([Attema et al., 2000](#)). The ERS-1 and ERS-2 had an incidence angle of 23° and were in tandem operation, meaning that ERS-2’s track would be the same as ERS-1’s with 24 hours delay, ([Duchossois and Martin, 1995](#)). ERS-1 and ERS-2 operated until March 2000 and June 2011, respectively ([Van’t-Klooster, 2011](#)).

ERS-1/2 level 1 SLC characteristics	
Pixel size	8m (slant range) x 4m (azimuth - along track)
Scene area	100 km (range) x at least 102.5 km (azimuth)
Number of looks	1
Total product volume	575 Mbytes/product

Table 1: ERS-1 and ERS-2 level 1 SLC’s image product characteristics ([ESA, 2017a](#)).

count	Satellite	Image(date)	Orbit
1	ERS 1	10/06/1993	9943
2	ERS 1	19/08/1993	10945
3	ERS 1	28/10/1993	11947
4	ERS 2	04/06/1995	634
5	ERS 2	09/07/1995	1135
6	ERS 2	13/08/1995	1636
7	ERS 2	17/09/1995	2137
8	ERS 2	31/12/1995	3640
9	ERS 2	19/05/1996	5644
10	ERS 2	23/06/1996	6145
11	ERS 2	10/06/1996	7648
12	ERS 2	11/10/1996	8149
13	ERS 2	06/08/1997	11155
14	ERS 2	17/08/1997	12157
15	ERS 2	21/09/1997	12658
16	ERS 2	19/04/1998	15664
17	ERS 2	24/05/1998	16165
18	ERS 2	28/06/1998	16666
19	ERS 2	06/09/1998	17668
20	ERS 2	28/02/1999	20173
21	ERS 2	13/06/1999	21676
22	ERS 2	18/07/1999	22177
23	ERS 2	22/08/1999	22678
24	ERS 2	26/09/1999	23179
25	ERS 2	31/10/1999	23680

Table 2: ERS-1 and 2 imagery (descending, track: 279, frame: 2835, polarization: VV) that has been used (in bold the master reference image).

count	Satellite	Image(date)	Orbit
1	ERS 1	29/04/1993	9349
2	ERS 1	03/06/1993	9850
3	ERS 2	28/05/1995	541
4	ERS 2	06/08/1995	1543
5	ERS 2	10/09/1995	2044
6	ERS 2	15/10/1995	2545
7	ERS 2	24/12/1995	3547
8	ERS 2	28/01/1996	4048
9	ERS 1	11/05/1996	25224
10	ERS 2	12/05/1996	5551
11	ERS 2	16/06/1996	6052
12	ERS 2	21/07/1996	6553
13	ERS 2	29/09/1996	7555
14	ERS 2	10/08/1997	12064
15	ERS 2	19/10/1997	13066
16	ERS 2	17/05/1998	16072
17	ERS 2	26/07/1998	17074
18	ERS 2	02/05/1999	21082
19	ERS 2	11/07/1999	22084
20	ERS 2	19/09/1999	23086
21	ERS 2	28/11/1999	24088

Table 3: ERS-1 and 2 imagery (ascending, track: 186, frame: 765, polarization: VV) that has been used.

6.2.2 ENVISAT

Envisat was at the time, Europe's the largest and most complex satellite and continued/extended the data services provided by ERS-1 and ERS-2. This satellite had Sun-synchronous polar orbit as well ([Dubock et al., 2001](#)), but the instruments were more complex than its' predecessors. Envisat had been

launched in 2002, had incidence angles 15-45° and its' mission ended in April 2012 (Kramer, 2017).

ENVISAT level 1 SLC characteristics	
Pixel size	8m (slant range) x 4m (azimuth - along track)
Scene area	100 km (range) x 56 to 100 km (azimuth)
Number of looks	1
Total product volume	741 Mbytes/product

Table 4: ENVISAT level 1 SLC's image product characteristics (ESA, 2016).

count	Satellite	Image(date)	Orbit
1	Envisat-1	22/06/2003	6846
2	Envisat-1	09/11/2003	8850
3	Envisat-1	22/02/2004	10353
4	Envisat-1	28/03/2004	10854
5	Envisat-1	11/07/2004	12357
6	Envisat-1	19/09/2004	13359
7	Envisat-1	13/03/2005	15864
8	Envisat-1	17/04/2005	16365
9	Envisat-1	13/11/2005	19371
10	Envisat-1	26/02/2006	20874
11	Envisat-1	11/06/2006	22377
12	Envisat-1	16/07/2006	22878
13	Envisat-1	29/10/2006	24381
14	Envisat-1	05/08/2007	28389
15	Envisat-1	27/01/2008	30894
16	Envisat-1	06/04/2008	31896
17	Envisat-1	11/05/2008	32397
18	Envisat-1	15/06/2008	32898
19	Envisat-1	20/07/2008	33399
20	Envisat-1	24/08/2008	33900

count	Satellite	Image(date)	Orbit
21	Envisat-1	28/09/2008	34401
22	Envisat-1	02/11/2008	34902
23	Envisat-1	07/12/2008	35403
24	Envisat-1	15/02/2009	36405
25	Envisat-1	22/03/2009	36906
26	Envisat-1	26/04/2009	37407
27	Envisat-1	31/05/2009	37908
28	Envisat-1	13/09/2009	39411
29	Envisat-1	22/11/2009	40413
30	Envisat-1	27/12/2009	40914
31	Envisat-1	07/03/2010	41916
32	Envisat-1	11/04/2010	42417
33	Envisat-1	20/06/2010	43419
34	Envisat-1	03/10/2010	44922

Table 5: Envisat-1 imagery (descending, track: 279, frame: 2835, polarization: VV) that has been used.

count	Satellite	Image(date)	Orbit
1	Envisat-1	11/02/2003	4978
2	Envisat-1	05/08/2003	7483
3	Envisat-1	14/10/2003	8485
4	Envisat-1	23/12/2003	9487
5	Envisat-1	06/04/2004	10990
6	Envisat-1	11/05/2004	11491
7	Envisat-1	20/07/2004	12493
8	Envisat-1	24/08/2004	12994
9	Envisat-1	28/09/2004	13495
10	Envisat-1	02/11/2004	13996
11	Envisat-1	11/01/2005	14998
12	Envisat-1	26/04/2005	16501
13	Envisat-1	31/05/2005	17002
14	Envisat-1	25/07/2006	23014
15	Envisat-1	03/10/2006	24016
16	Envisat-1	16/01/2007	25519
17	Envisat-1	20/02/2007	26020
18	Envisat-1	11/03/2008	31531
19	Envisat-1	15/04/2008	32032
20	Envisat-1	29/07/2008	33535
21	Envisat-1	02/09/2008	34036
22	Envisat-1	07/10/2008	34537
23	Envisat-1	11/11/2008	35038
24	Envisat-1	20/01/2009	36040
25	Envisat-1	24/02/2009	36541
26	Envisat-1	05/05/2009	37543
27	Envisat-1	09/06/2009	38044
28	Envisat-1	09/02/2010	41551

Table 6: Envisat-1 imagery (ascending, track: 415, frame: 765, polarization: VV) that has been used.

6.2.3 TerraSAR-X

TerraSAR-X is a commercial German SAR Earth observation satellite launched in June 2007 expected to deliver data beyond 2018. This satellite is equipped with a high frequency X-band SAR sensor, in a Sun-synchronous repeat orbit and with incidence angle range from 15° to 60° ([Airbus Defence and Space, 2014](#)).

TerraSAR-X Strip Map SSC, single polarization characteristics	
Pixel size	1.2m (slant range) x 3.3m (azimuth - along track)
Scene area	30 km (range) x 50 km (azimuth)
Number of looks	1
Total product volume	1.95 Gbytes

Table 7: TerraSAR-X, StripMap (SM), single polarization, level 1 SLC's image product characteristics ([Airbus Defence and Space, 2014](#)).

count	Satellite	Image(date)	Orbit
1	TerraSAR-X	30/11/2010	19199
2	TerraSAR-X	11/12/2010	2636
3	TerraSAR-X	22/12/2010	2803
4	TerraSAR-X	02/01/2011	2970
5	TerraSAR-X	13/01/2011	19867
6	TerraSAR-X	04/02/2011	20201
7	TerraSAR-X	15/02/2011	3638
8	TerraSAR-X	26/02/2011	20535
9	TerraSAR-X	09/03/2011	3972
10	TerraSAR-X	20/03/2011	20869

count	Satellite	Image(date)	Orbit
11	TerrraSAR-X	31/03/2011	4306
12	TerrraSAR-X	11/04/2011	4473
13	TerrraSAR-X	03/05/2011	4807
14	TerrraSAR-X	14/05/2011	4974
15	TerrraSAR-X	25/05/2011	21871
16	TerrraSAR-X	27/06/2011	22372
17	TerrraSAR-X	10/08/2011	6310
18	TerrraSAR-X	21/08/2011	23207
19	TerrraSAR-X	15/10/2011	24042
20	TerrraSAR-X	26/10/2011	24209
21	TerrraSAR-X	06/11/2011	7646
22	TerrraSAR-X	17/11/2011	7813
23	TerrraSAR-X	09/12/2011	24877
24	TerrraSAR-X	11/01/2012	25378
25	TerrraSAR-X	28/03/2012	26547
26	TerrraSAR-X	08/04/2012	26714
27	TerrraSAR-X	19/04/2012	10151
28	TerrraSAR-X	30/04/2012	27048
29	TerrraSAR-X	02/06/2012	27549
30	TerrraSAR-X	24/06/2012	27883
31	TerrraSAR-X	07/08/2012	28551
32	TerrraSAR-X	29/08/2012	28885

Table 8: TerraSAR-X imagery (ascending, relative orbit: 161, polarization: HH) that has been used.

6.2.4 Sentinel-1

ESA's heritage of C-band SAR systems (ERS-1, ERS-2 and Envisat) continues with Sentinel-1 A and B, two satellites orbiting 180° apart. Sentinel-1A and B were launched with 2 years delay, in April 2014 and in April 2016 respectively (ESA, 2017c). These satellites use an interferometric wide swath mode

which obtains three sub-swaths using Terrain Observation with Progressive Scans SAR (TOPSAR) technique, with several bursts per sub-swath, in a range of incidence angle from 29.1° to 46.0° (ESA, 2017b).

Sentinel-1 level 1 Interferometric Wide Swath SLC characteristics	
Pixel size	5m (range) x 20m (azimuth)
Scene area	250km swath width
Sub-swaths	3
Number of looks	1
Total product volume	8 GB/product

Table 9: Sentinel-1 level 1 SLC's image product characteristics (ESA, 2017b).

count	Satellite	Image(date)	Orbit
1	Sentinel-1A	27/01/2015	4352
2	Sentinel-1A	08/02/2015	4527
3	Sentinel-1A	04/03/2015	4877
4	Sentinel-1A	16/03/2015	5052
5	Sentinel-1A	28/03/2015	5227
6	Sentinel-1A	09/04/2015	5402
7	Sentinel-1A	17/12/2015	9077
8	Sentinel-1A	29/12/2015	9252
9	Sentinel-1A	10/01/2016	9427
10	Sentinel-1A	22/01/2016	9602
11	Sentinel-1A	03/02/2016	9777
12	Sentinel-1A	15/02/2016	9952
13	Sentinel-1A	27/02/2016	10127
14	Sentinel-1A	10/03/2016	10302
15	Sentinel-1A	03/04/2016	10652
16	Sentinel-1A	15/04/2016	10827
17	Sentinel-1A	08/07/2016	12052
18	Sentinel-1A	01/08/2016	12402

count	Satellite	Image(date)	Orbit
19	Sentinel-1A	13/08/2016	12577
20	Sentinel-1A	30/09/2016	13277
21	Sentinel-1B	06/10/2016	2381
22	Sentinel-1A	12/10/2016	13452
23	Sentinel-1B	18/10/2016	2556
24	Sentinel-1A	24/10/2016	13627
25	Sentinel-1B	30/10/2016	2731
26	Sentinel-1A	05/11/2016	13802
27	Sentinel-1A	17/11/2016	13977
28	Sentinel-1A	29/11/2016	14152
29	Sentinel-1A	11/12/2016	14327
30	Sentinel-1A	23/12/2016	14502
31	Sentinel-1A	04/01/2017	14677
32	Sentinel-1A	16/01/2017	14852
33	Sentinel-1A	28/01/2017	15027
34	Sentinel-1A	09/02/2017	15202
35	Sentinel-1A	21/02/2017	15377
36	Sentinel-1A	05/03/2017	15552
37	Sentinel-1A	17/03/2017	15727
38	Sentinel-1A	29/03/2017	15902
39	Sentinel-1A	10/04/2017	16077
40	Sentinel-1A	22/04/2017	16252
41	Sentinel-1A	04/05/2017	16427
42	Sentinel-1B	10/05/2017	5531
43	Sentinel-1A	16/05/2017	16602
44	Sentinel-1B	22/05/2017	5706
45	Sentinel-1A	09/06/2017	16952
46	Sentinel-1A	21/06/2017	17127

Table 10: Sentinel-1 imagery (descending, track: 80, frame: 463) that has been used.

count	Satellite	Image(date)	Orbit
1	Sentinel-1A	30/09/2015	7947
2	Sentinel-1A	17/11/2015	8647
3	Sentinel-1A	3/05/2016	11097
4	Sentinel-1A	27/05/2016	11447
5	Sentinel-1A	2/07/2016	11972
6	Sentinel-1A	14/07/2016	12147
7	Sentinel-1A	7/08/2016	12497
8	Sentinel-1A	6/10/2016	13372
9	Sentinel-1A	18/10/2016	13547
10	Sentinel-1A	30/10/2016	13722
11	Sentinel-1A	11/11/2016	13897
12	Sentinel-1A	23/11/2016	14072
13	Sentinel-1A	5/12/2016	14247
14	Sentinel-1A	29/12/2016	14597
15	Sentinel-1A	10/01/2017	14772
16	Sentinel-1A	22/01/2017	14947
17	Sentinel-1A	3/02/2017	15122
19	Sentinel-1A	15/02/2017	15297
20	Sentinel-1A	27/02/2017	15472
21	Sentinel-1A	11/03/2017	15647
22	Sentinel-1A	23/03/2017	15822
23	Sentinel-1A	4/04/2017	15997
24	Sentinel-1A	16/04/2017	16172
25	Sentinel-1A	28/04/2017	16347
26	Sentinel-1A	10/05/2017	16522
27	Sentinel-1A	22/05/2017	16697
28	Sentinel-1A	3/06/2017	16872
29	Sentinel-1A	15/06/2017	17047
30	Sentinel-1A	27/06/2017	17222

Table 11: Sentinel-1 imagery (ascending, track: 175, frame: 122) that has been used.

7 Methodology

The multi-temporal observation of the Patra-Rio region was done by DInSAR techniques. The algorithms used were the SVD (Berardino et al., 2002) and IPTA approach (Osmanoglu et al., 2015). Both of the approaches are well known to the scientific community, however each resolves DInSAR problems from different perspectives.

Throughout the dissertation, three software have been used. All processing was carried out with the use of the GAMMA Remote Sensing Software. This software supports the SAR, InSAR and DInSAR processing of remote SAR systems. Then the results were imported to ArcGIS, a mapping & analytics platform for data manipulation and the illustration of the results with maps. Finally, some diagrams were made with the Microsoft Excel 2016 spreadsheet software.

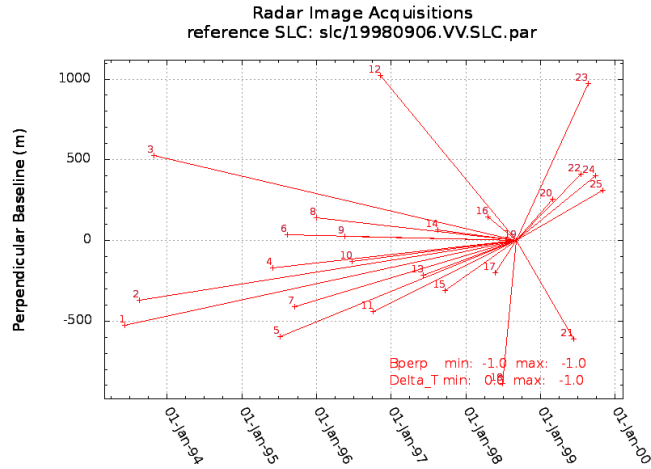
7.1 PSs method - IPTA algorithm

7.1.1 IPTA pre-processing

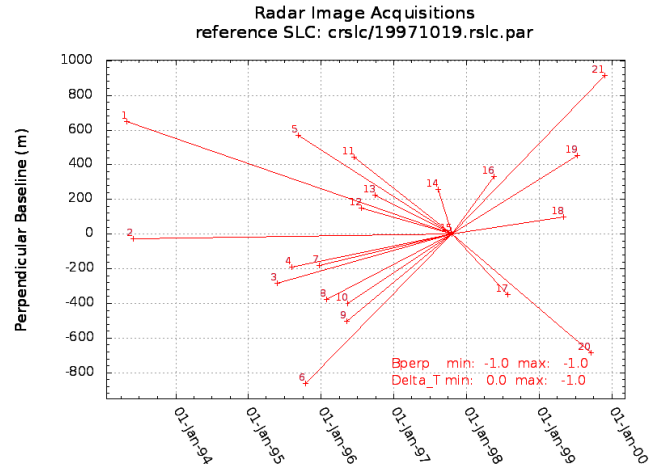
The first step is from the advanced SAR data to generate the SLC parameter and image files. The next step is to replace the single state vector provided with the SLC data with precision state vectors as to calculate or update the orbit parameters of the SLC parameter file. Afterwards, an initial lookup table, simulated SAR image, and DEM segment parameters have to be generated to determine if the DEM has enough detail for geocoding.

When all data are on the right format, the coregistration can be achieved. Here, all slave images will be reasmpled to the geometry of tha master image. The IPTA technique demands choosing the optimal master product which will give the average perpendicular baseline closest to zero. The reference scene was selected primarily on the baseline minimization criteria, however, it is of interest to choose the reference scene near the temporal average of the available SAR acquisitions. The average perpendicular baseline per IPTA analyzed data-set, as seen in Figure 20, are: (a) -23.379m, (b) 12.683m, (c) -25.208m, (d) 53.347m and (e) -26.617m.

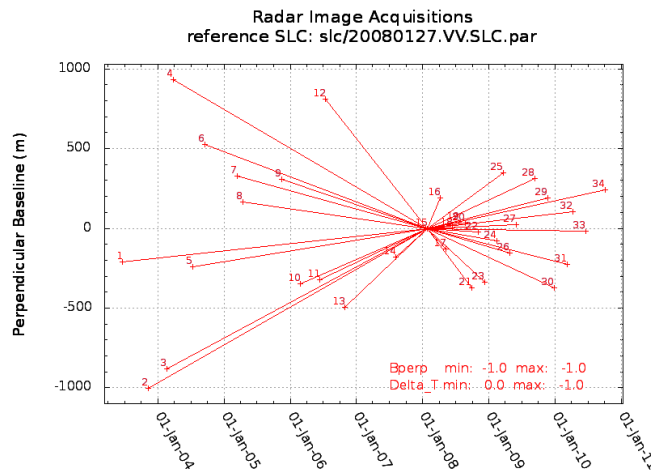
From this point, in order to economise resources and remove unnecessary information, the SLC images can be cropped and keep only the studied subset.



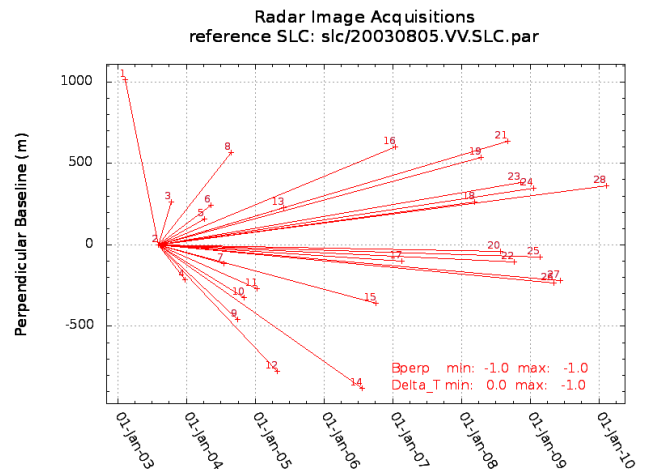
(a) ERS descending



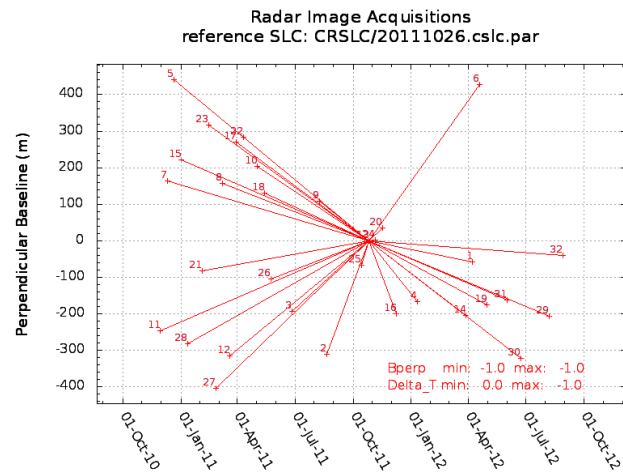
(b) ERS ascending



(c) Envisat descending



(d) Envisat ascending



(e) TerraSAR-X ascending

Figure 20: Plots of acquisition dates versus the baselines of the interferograms.

7.1.2 IPTA processing

The processing commences with the selection of the point targets, probable PSs with low spectral phase diversity and/or low intensity variability, expecting that PSs should not show speckle behavior since the dominant scatterer would produce simple coherent echoes. From these points some are excluded from the processing due to coherence and mean sigma ratio thresholds that are applied. The thresholds over these probable PSs do not ensure the appearance of points over flat areas, on the contrary, probable PSs may be shown over mountainous regions as well as on water surfaces.

Following comes the generation and analysis of point data stack of differential interferograms by means of phase regression analysis in the temporal domain. A two dimensional bi-linear analysis is done with the dimensions corresponding to the perpendicular baseline of each interferometric pairs and to the time difference between the two images, as in:

$$a_0 + a_1 * b_{perp}[i] + a_2 * delta_t[i] \quad (10)$$

where a_0 is the phase offset, a_1 is the slope baseline dimension, a_2 is the slope in time dimension, b_{perp} is the perpendicular baseline component and $delta_t$ is the time interval of the $[i]$ interferograms.

The inspection of linear dependence of the topographic phase to the perpendicular baseline and of linear phase dependence with time, will lessen the impact of distance between the two pairs phase components. Such components are the atmospheric distortion, the baseline error and higher relative deformation rates in individual points with higher deviations from the regression plain. Afterwards, an evaluation of the preliminary probable PSs is needed in order to reject the ones with phase standard deviation larger than the desired threshold. As a result, an important number of PSs candidates that will be rejected used to be located over water surface or mountainous areas.

Following comes the choice of the reference point for unwrapping, which in this study is the area in proximity with the GNSS permanent station of Patras' University (PAT0). The unwrapped interferometric phase is the same as in conventional interferometry, well expressed by (Werner et al., 2003) as:

$$\Phi_{unw} = \phi_{topo} + \phi_{disp} + \phi_{atm} + \phi_{noise} \quad (11)$$

very similar to the equation (1), however the orbital phase errors and the flat earth phase component have been dealt with.

From the unwrapped phases, some PS points express ground movement close to none and these are used for a baseline refinement. With the refined baselines, height corrections and estimated linear deformation rates, the interferometric model of the phase was revised.

Furthermore, the results were treated with temporal and spacial filters in order to minimise atmospheric and other noises. Considering atmospheric effects as of large scale and non-linear, a spatial filter of linear least-squares was applied so that non-linear deformation at scales larger than approximately 400m on ground were removed. Additionally, as atmospheric effects and other noises are not correlated temporally another filter was used calculating combined atmospheric corrections for the interferometric pairs. Additional phase noise was decreased with spatial average filtering around the reference point, presuming no ground deformation in the area.

From this step, only points with very low standard deviation from the regression functions will undertake point-wise investigation of the baseline and time dependence of the interferometric phase. For these points height corrections, linear displacement rates and residual phases will be estimated.

Lastly, small scale linear least-squares spatial filtering of the residual phases has been used to suppress phase noise and non-linear movement over multiple observation has been removed with temporal filtering. Temporal filtering with linear regression reduces errors from the interferograms with the largest temporal baselines,

Results of this technique are PSs heights, linear ground movement rates, atmospheric phase, refined baselines, phase coherence measurements for quality control, non-linear deformation histories for each point and linear displacement rates of PSs on the LOS.

7.2 Hybrid method - SVD algorithm

The SVD processing has been applied only on the Sentinel-1 data and thus the steps explained would be a little different if it were for another satellite. The differences come from the bursts and sub-swaths of Sentinel-1 imagery and the unprecedentedly small baselines between the acquisitions.

7.2.1 SVD pre-processing

Firstly, in the interest of saving some memory space and make the procedure faster, the sub-swaths and bursts containing the area were defined as to compute the multi-temporal analysis only with them.

Afterwards, an image from the data-set (later defined as master image) has to be terrain geocoded and the DEM has to be re-sampled to SAR Range-Doppler Coordinates. Through this all other, slave Sentinel-1 TOPS SLCs can be coregistered to the master - reference burst. This step is essential to be done on less than a pixel's offset so that pixel by pixel calculations are valid.

Then, the coregistration takes place where the slave images are resampled to the master's geometry. With orbit geometry and terrain height a coregistration lookup table is calculated. This table is refined with intensity matching and the spectral diversity methods. This automated procedure refines the table until azimuth correction reaches <0.01 pixel and azimuth coregistration with spectral diversity is <0.0005 pixel. In context of reserving more memory space and accelerate the process, the images are cut with specific boundaries on the area of interest.

As all images are now coregistered, interferogram pairs with specific perpendicular and temporal baseline can be computed (Fig. 21). For the maximum scene number difference between passes of 3: Figure (21a) illustrates 132 pairs of average perpendicular baseline 59.095m, and Figure (21b) illustrates 81 pairs of average perpendicular baseline 46.136 m.

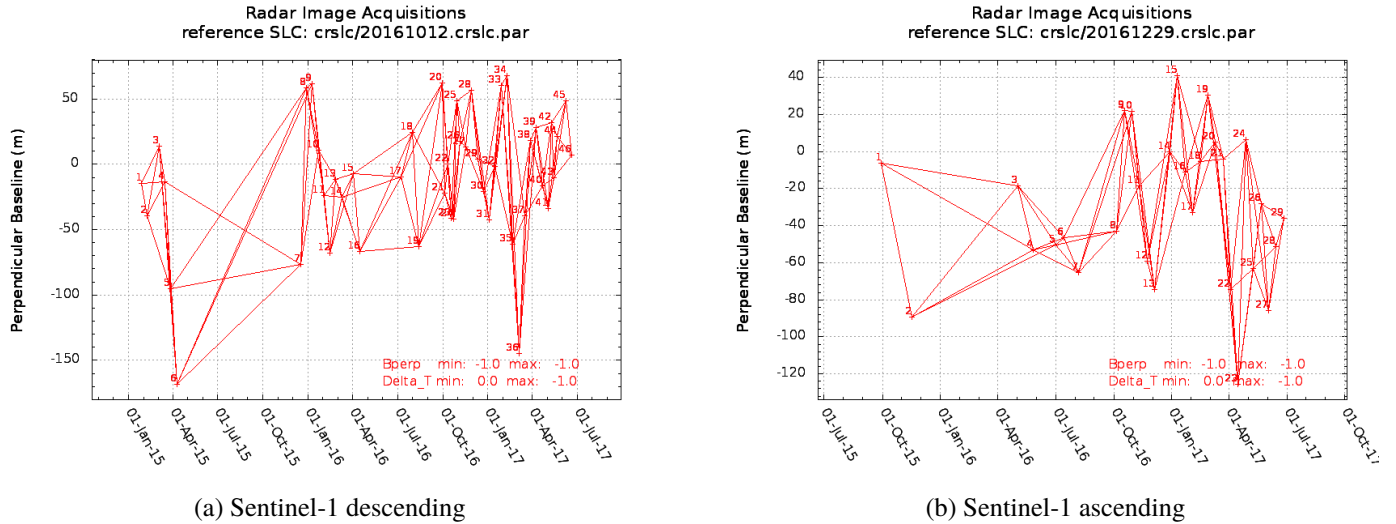


Figure 21: Plots of acquisition dates versus the baselines of the interferograms.

For interferometric pairs of relatively small perpendicular baseline, the wrap interferograms are calculated. From each interferogram, the flat Earth component is removed and same goes for the topographic phase. Subsequently an adaptive filtering of the set of differential intrferograms is benevolent for phase noise reduction. These wrap interferograms produced with the GAMMA software are believed to be satisfying enough to unwrap them with a minimum cost flow algorithm. The unwrapping took reference point near the permanent GNSS station of the University of Patras ([PAT0](#)) . With the unwrapped phases and the DEM, precision baselines are calculated and are used for a second pass of wrapping, adaptive filtering and unwrapping, leading to more robust results.

7.2.2 SVD processing

For the set of multi-reference continuous unwrapped interferograms, the time-series phase and it's linear fit are calculated. From the linear fit and the unwrapped interferograms, displacement maps on LOS can be estimated.

Finally, the displacement rates are geocoded to the geographical projection of the desired digital elevation model. In order to further distribute and manage the results, the geocoded data were converted into a GeoTIFF file.

8 Results

The results are illustrated with maps for better understanding of the spatial extent and geographic location of each feature. Moreover, each map contains information for the line-of-sight of a specific satellite and either its ascending or descending orbits. Even though the satellites are different, the angle for their line-of-site is similar and such that the motion observed is mostly vertical ([Samieie-Esfahany et al., 2009](#)). Lastly, all maps contain the faults seen in Figure (16) as to compare the dissertation's findings to the literature's. The results of categorised data-sets are as following:

ERS descending, Figure 22. The feature north of the PRFZ is slightly dipping relatively to the reference point. The same feature is gradually dipping towards the north. More points seem stable at the port.

ERS ascending, Figure 23. The marked PRFZ separates clearly a stable (southern) feature and a dipping one (northern feature). The buildings around the port of Patras function great as scatterers and those close to the PRFZ and south of it, stay stable over the years observed (relatively to the reference point).

Envisat descending, Figure 24. PRFZ aligns with the boundaries of blocks moving independently. The feature north of PRFZ is moving away from the satellite, with bigger rate of motion in its center. Additionally, at the SW part of the down-throwing (northern) feature, a difference in motion rate indicates the existence of possible fault perpendicular to the PRFZ.

Envisat ascending, Figure 25. Southern to the PRFZ the points are more stable or dip with smaller rate than the points norther to the fault zone. Most motion occurs at the central part of the northern block.

TerraSAR-X ascending, Figure 26. Due to unwrapping errors, the studied area with the x-band data had to be smaller than the areas studied by the other satellites. South of the PRFZ, points are relatively stable or uplifting compared to the reference point on the LOS. North of the PRFZ, the points are both uplifting and dipping, however the dipping points outnumber the uplifting ones.

Sentinel-1 descending, Figure 27. Ground motion comes in accordance with the literature review. PRFZ and other faults are clearly seen by the patterns made of motion rate differences. Though, most dipping motion is observed towards smaller altitude - the shore.

Sentinel-1 ascending, Figure 28. As pointed in the map, PRFZ is separating a more stable southern block from a dipping northern one. For the dipping block, bigger motion rate is at its center and motion rate differences at the SW part lead to assumptions of fault perpendicular to the PRFZ.

Feature north of PRFZ, Figure 29. Distribution curves for the ground motion observed by all the satellites show that this feature is moving away from the satellites. Nonetheless, the results obtained by the ascending orbits (brown and green lines) have distribution curves with picks pointing greater motion away from the satellites than the picks of the descending data-sets (blue lines). It is also note worthy that the motion away from the satellites is gradually augmenting with the passage of time (illustrated with lighter to darker colours for oldest to newer data-sets of same orbital direction and bandwidth).

Feature south of PRFZ, Figure 30. Distribution curves for the ground motion observed by all the satellites show that this feature is more stable from the southern feature. For the distribution curves of all the data-sets, no patterns can be recognised.

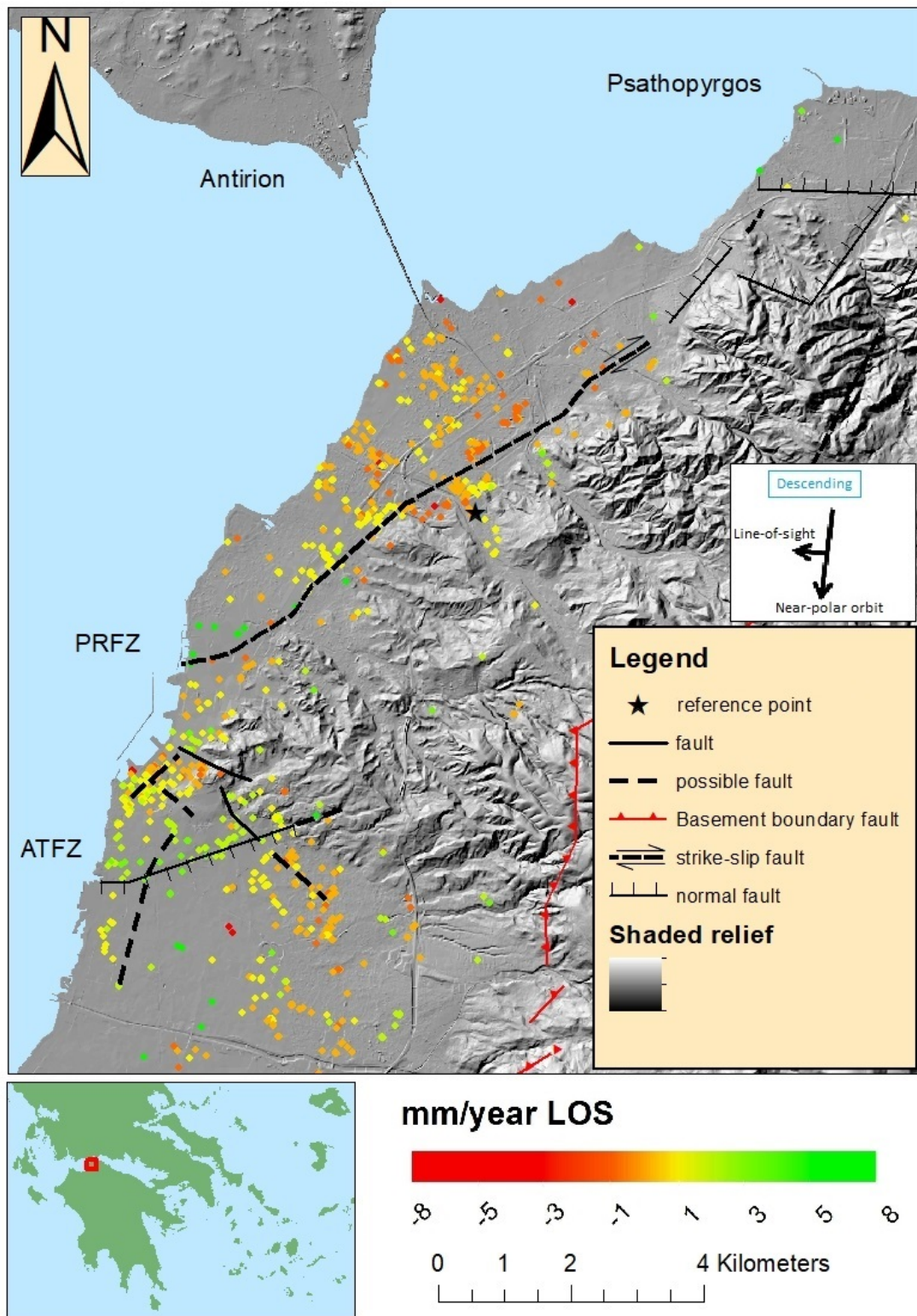


Figure 22: IPTA results for the ERS descending data-set. Values < -8 or > 8 mm/year, that consist $< 10\%$ of the overall results, have been excluded.

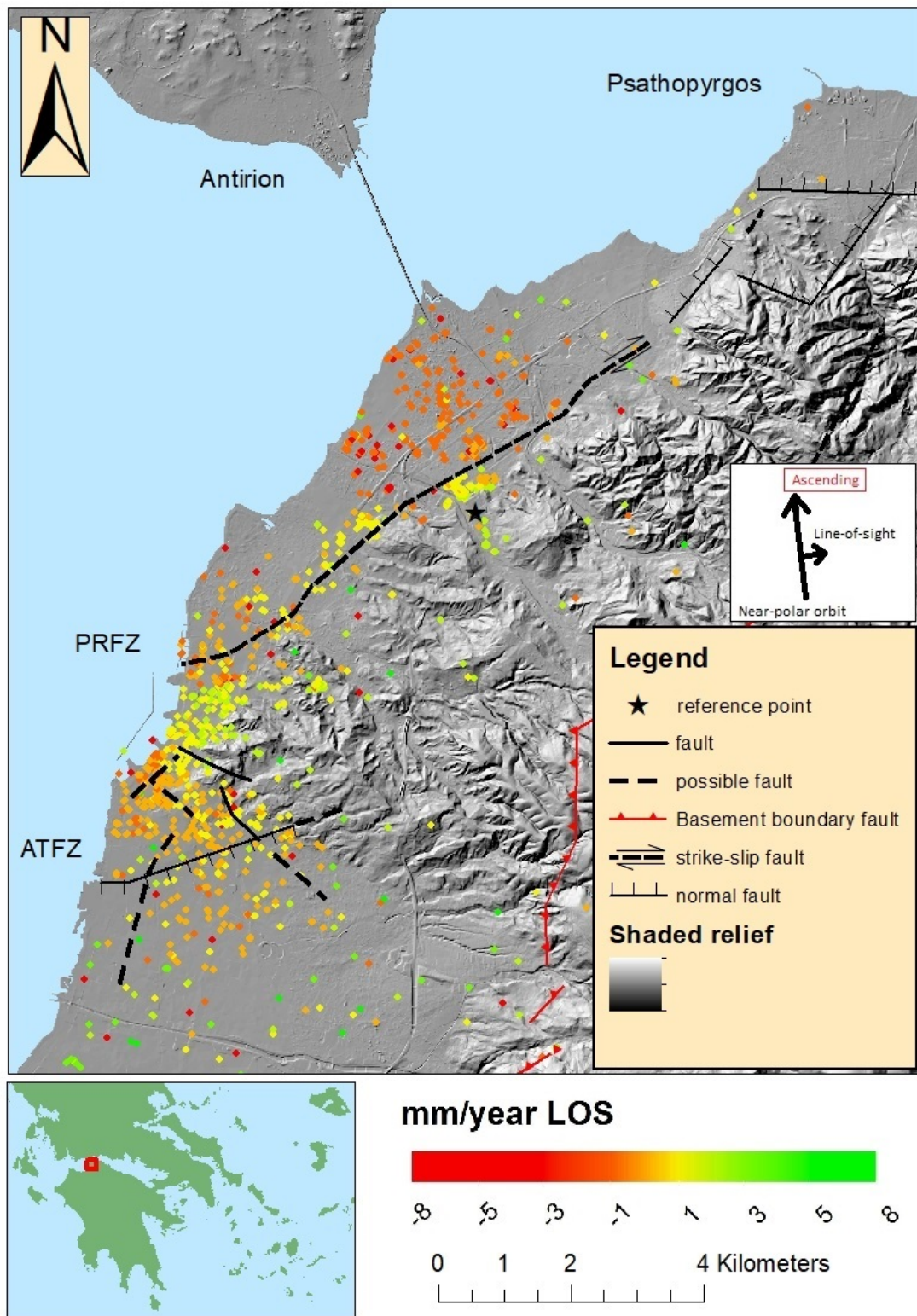


Figure 23: IPTA results for the ERS ascending data-set. Values < -8 or > 8 mm/year, that consist $< 10\%$ of the overall results, have been excluded.

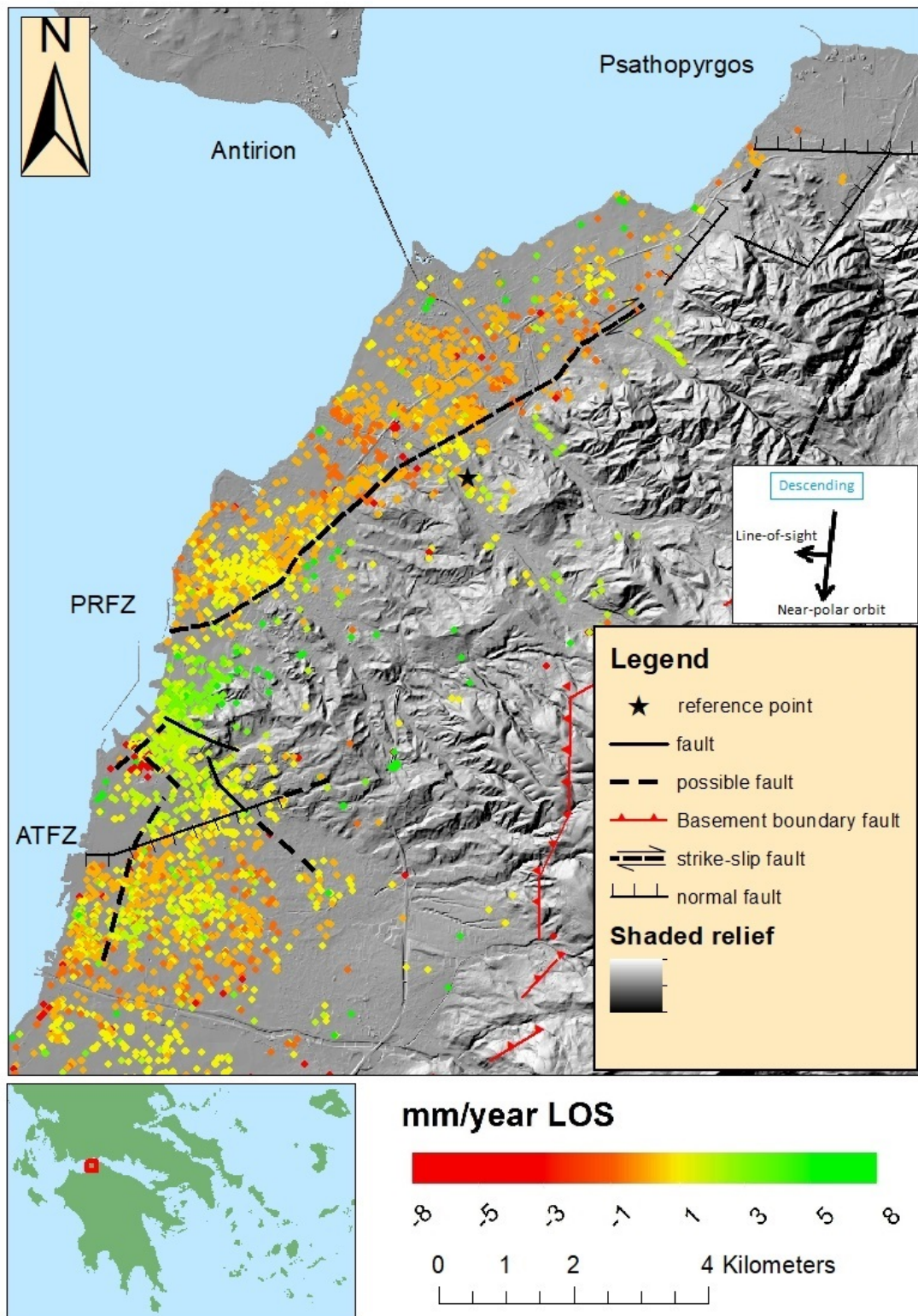


Figure 24: IPTA results for the Envisat descending data-set. Values < -8 or > 8 mm/year, that consist $< 10\%$ of the overall results, have been excluded.

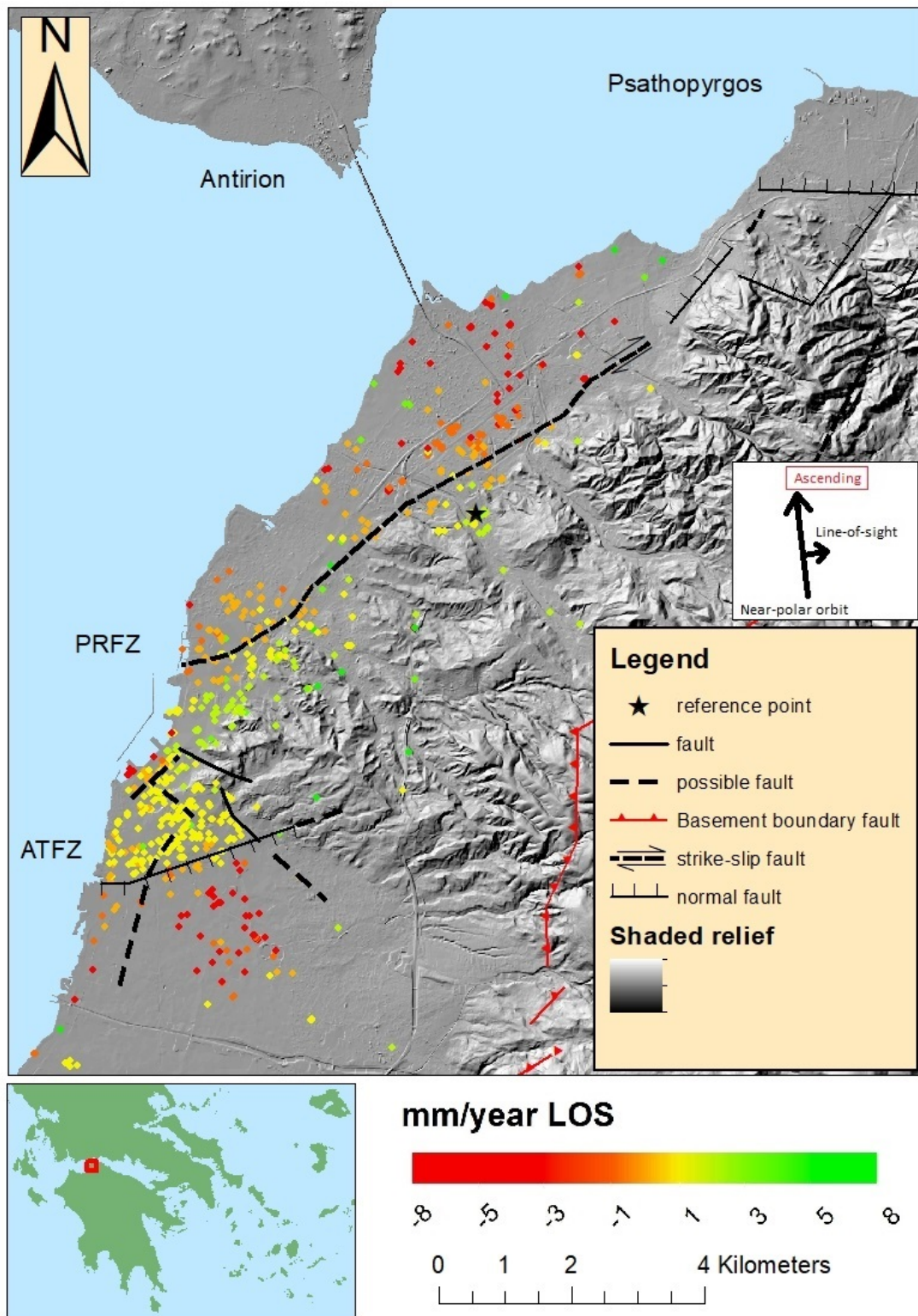


Figure 25: IPTA results for the Envisat ascending data-set. Values < -8 or > 8 mm/year, that consist $< 10\%$ of the overall results, have been excluded.

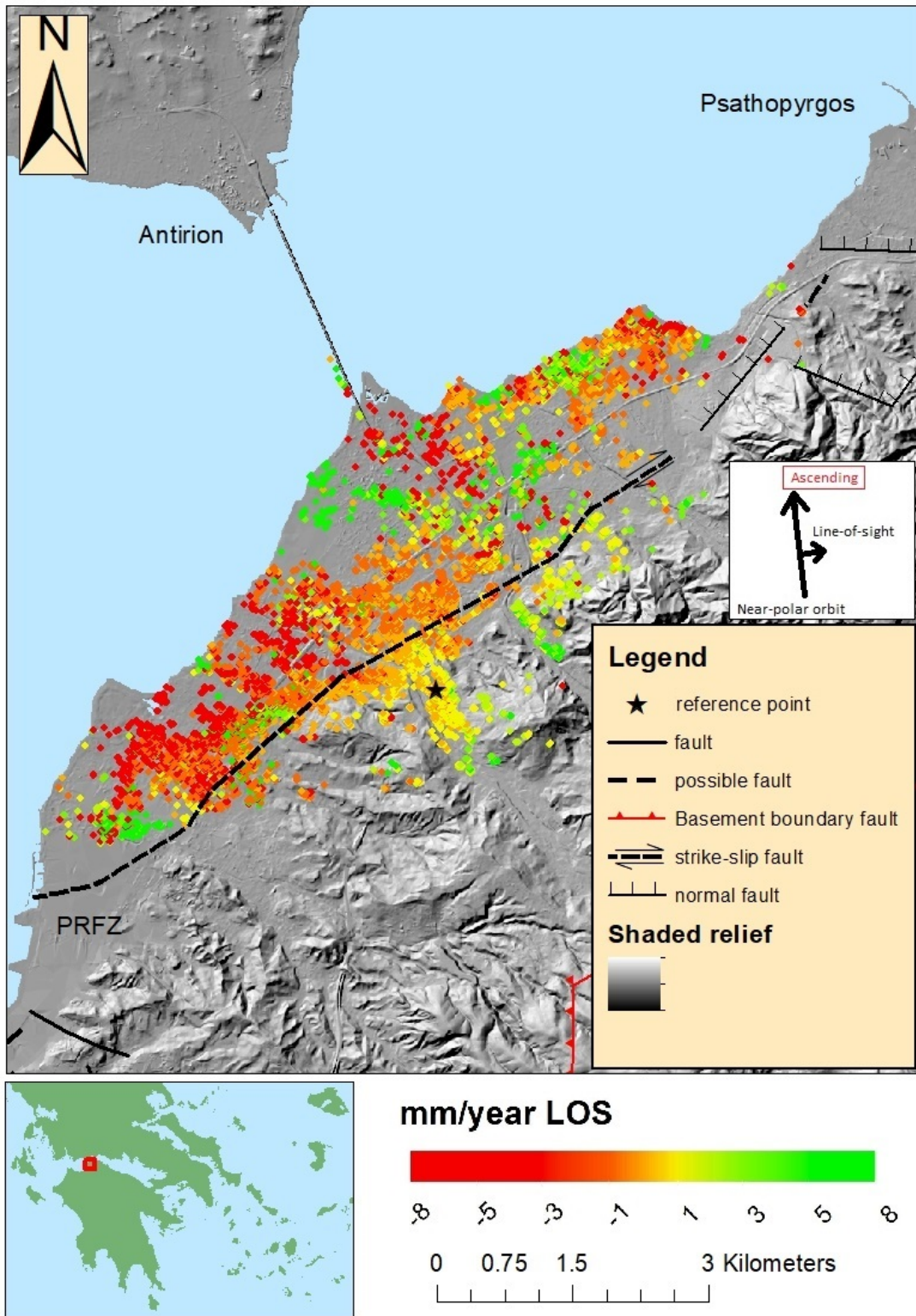


Figure 26: IPTA results for the TerraSAR-X ascending data-set. Values < -8 or > 8 mm/year, that consist $< 16\%$ of the overall results, have been excluded.

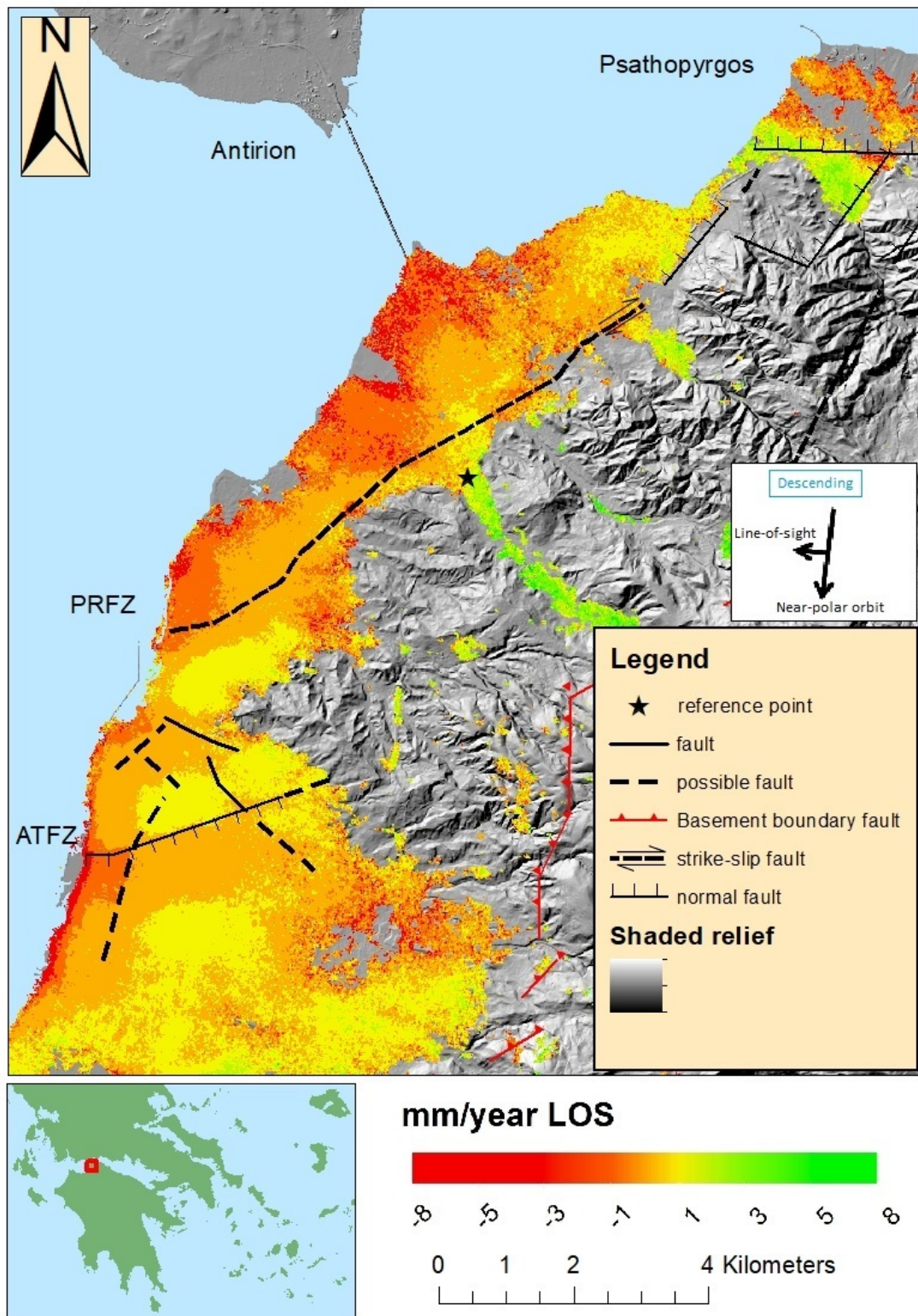


Figure 27: SVD results for the Sentinel-1 descending data-set. Values < -8 or > 8 mm/year, that consist $< 10\%$ of the overall results, have been excluded.

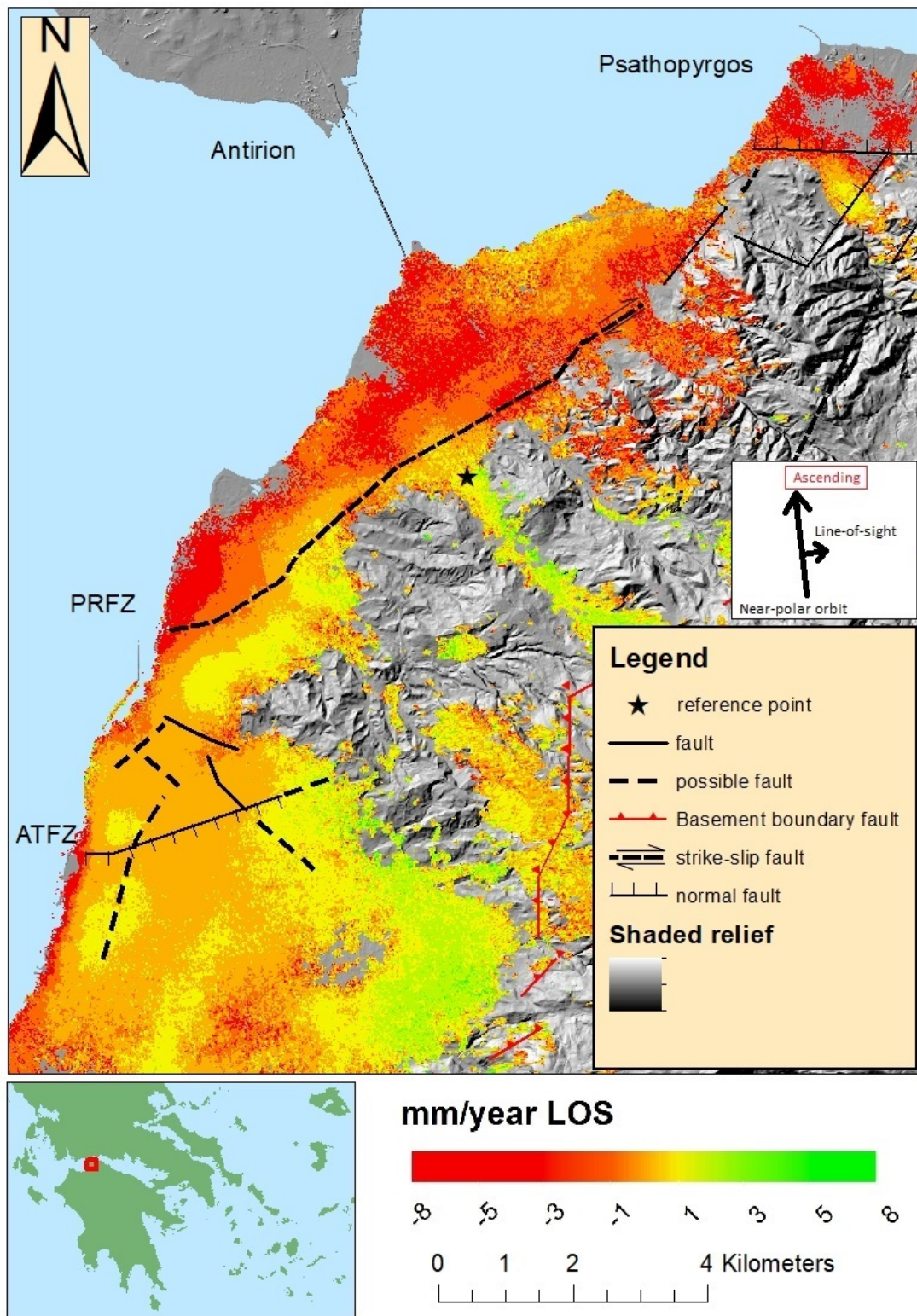


Figure 28: SVD results for the Sentinel-1 ascending data-set. Values < -8 or > 8 mm/year, that consist $< 10\%$ of the overall results, have been excluded.

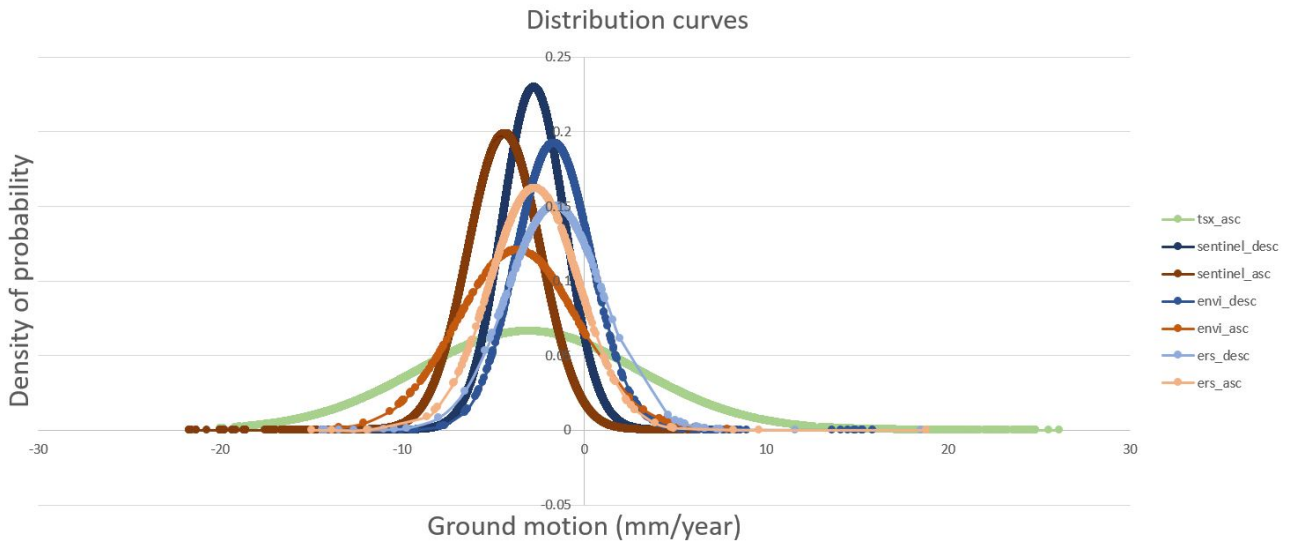


Figure 29: Distribution curves for the northern feature of PRFZ.

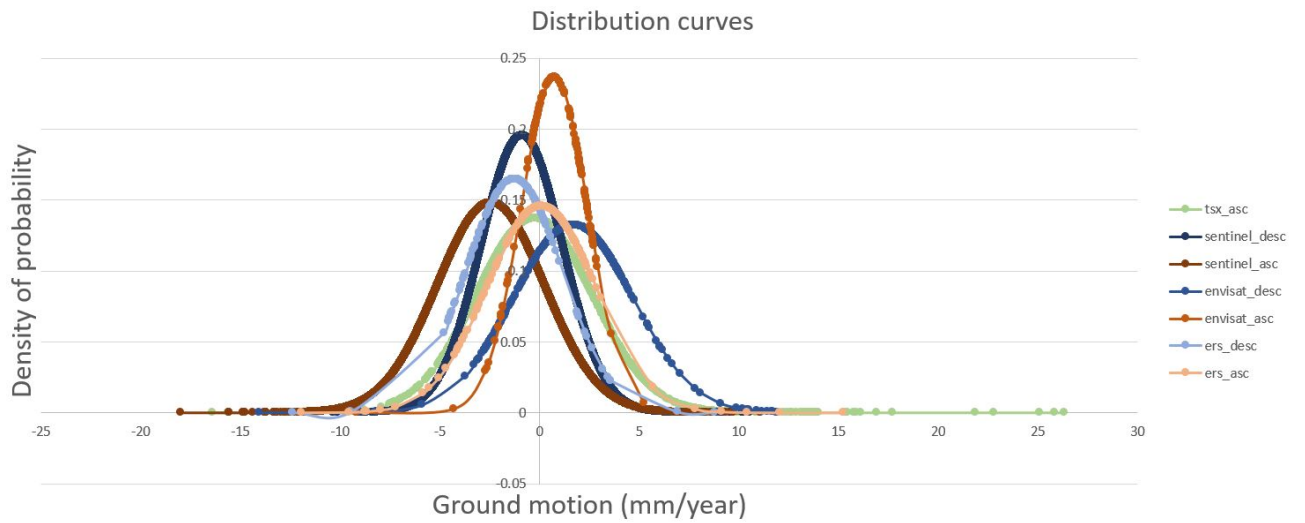


Figure 30: Distribution curves for the southern feature of PRFZ.

9 Discussion

Over the 1993 to 2017 period, the expansion of the city, the stratigraphy and the tectonics have contributed to the ground motion presented in this thesis.

For all data-sets of the same orbital direction (ascending/descending), similar deformation patterns have been identified. Since almost identical trends are observed over distinctive time lines, it is justifiable to assume a linear trend also over the interval not recorded by the SAR data. A linear trend persistent in such a long period (04/1993 up to 06/2017) permits the assumption of ground motion due to the same causes. However not all motions can be justified by only one cause since more causes can contribute to the same motion.

Comparing the ascending with the descending orbits, some motion is common while some is recorded in different extent. Places showing the same amount and direction of motion for descending and ascending orbits corroborate the results and express mostly vertical motion. However over the PRfz, the time-series analysis demonstrates partially, stronger motion observed by the ascending orbits than for the descending ones. If we assume that the PRfz is a normal fault, the hanging wall expresses less amount of motion away from the descending orbit than it does for the ascending one. Taking into consideration that the descending orbits have a west looking slant-range direction, and the ascending orbits have an east looking slant-range direction, the difference in linear motions observed can be interpreted as horizontal East-West motion.

Comparing results of the same orbital direction (ascending/ascending or descending/descending) diachronically. North of the PRfz, as the data-set analyzed becomes more recent, more PSs show greater motion away from the satellite. Figure 29 illustrates that the probability of points with greater motion away from the satellite augments. Again, it is reminded that motion on the LOS does not correspond to only tectonic motion; nonetheless, the ground motion is not stationary with time and should be studied in depth.

Other normal or reverse faults can be identified from the opposite motion direction of neighboring blocks, equally seen from both orbital directions of the satellite. Characteristically for faults, one block moves away from the satellite and the other block is moving towards the satellite. Moreover, the boundaries of blocks identified by DInSAR means coincide with older fault cartography.

The resulting maps have different amounts of permanent scatterers and coherence. For the IPTA processing, comparing the maps with the corresponding average perpendicular baseline of each dataset, a negative correlation can be observed between amount of PSs and average perpendicular baseline. For both IPTA and SVD processing, the results show more apparent ground motion when more images are used, expressing positive correlation. Moreover, differences among deformation patterns could result from the different viewing geometries of each satellite. Worth noting are the differences between the TerraSAR-X and Sentinel-1 ascending results. Even though the amount of images and time covered are similar, the results have dissimilarities due to unwrapping errors, different atmospheric contributions, polarization and bands used. Lastly, the conclusions made do not refer to each point separately but to the overall result.

10 Conclusions

A relatively new approach for remote active fault monitoring has been applied to the Patra-Rio fault zone in order to better understand the tectonics of the area and the risk occurring for the urban and sub-urban areas of the region. The multi-temporal DInSAR techniques can be carried out rapidly, with minimum cost when data of open access are used, over large areas and most importantly even on areas where no previous research has been conducted due to the vast coverage of satellite imagery. In multi-temporal interferometry, the precision of the results augments with the increasing number of images processed. Data from different satellites have been used in order to increase the temporal coverage analyzed, with each satellite data-set corresponding to a specific period of years.

The resulting maps illustrate mostly ground motion from -8 to 8 mm/year on the LOS, with better coherence being observed on urban and sub-urban areas, where buildings become scatterers of the satellite emitted waves. The linear movements from 1993 to 2017 lead to the conclusion of active tectonics, surely of strike-slip component (of approximately 2-3mm/year motion rate) and very possibly of normal faults as well. In this case the PRFZ would be consisted of oblique right-lateral faults and other active surrounding faults, characterized by the literature review as normal. However, from the motion observed on the LOS, faults in close proximity of the city are only one of the components resulting to displacement.

Even though in this dissertation a large amount of data was processed for the area, there is still much room for future research. Troubling is the fact that the ground north of the PRFZ seems to be accelerating its motion. Superior analysis could be achieved with the study of even more images and the use of a wider number of data providers.. Obviously, conducting the same research for other areas would provide further knowledge on the tectonics and the geo-hazards in the studied areas. However, more experimentation on the various DInSAR techniques and satellite imagery can be operated on the western Gulf of Corinth. This natural laboratory of active tectonics can be used to evaluate and compare different algorithms of SAR data analysis.

References

- Θεοδοσίου, Χ. (2015). Ενεργά ρήγματα στον αστικό πολεοδομικό ιστό. *Master's thesis*.
- Θεοδωρακόπουλος, Π. Κ. (2015). Γεωλογική δομή της περιοχής του αστικού συγκροτήματος Πατρών - γεωτεχνικός χαρακτηρισμός στις θέσιες του αστικού δικτύου επιταχυνσιογράφων UPAN. *Master's thesis*.
- Νόρδα, Μ. Ε. (2015). Ανάλυση και επεξεργασία μετρήσεων σεισμικού θορύβου και εφαρμογή στην περιοχή του Ρίου. *Master's thesis*.
- Παρχαρίδης, Ι. (2015). Αρχές δορυφορικής τηλεπισκόπησης Θεωρία και Εφαρμογές. *HEALLINK*.
- Ρόζος, Δ. (1989). Τεχνικογεωλογικές συνθήκες στο Νομό Αχαΐας, Γεωμηχανικοί χαρακτήρες Πλειοπλειοστοκαινικών ιζημάτων. *PhD thesis*.
- Τσόδουλος, Ι. Μ. (2009). Ενεργός Τεκτονική της ΝΑ Στερεάς Ελλάδας. *PhD thesis*.
- Abdelfattah, R. (2009). *Advances in Geoscience and Remote Sensing*, chapter InSAR phase analysis: Phase unwrapping for noisy SAR interferograms, pages 419–439. *InTech*.
- Airbus Defence and Space (2014). *TerraSAR-X Image Product Guide*, 2.0 edition.
- Alam, N., Alam, M. S., and Tesfamariam, S. (2012). Buildings' seismic vulnerability assessment methods: a comparative study. *Natural Hazards*, pages 405–424.
- Amato, V., Aucelli, P. P., Sessa, E. B., Cesarano, M., Incontri, P., Valente, G. P. E., and Vilardo, G. (2017). Multidisciplinary approach for fault detection: Integration of PS-InSAR, geomorphological, stratigraphic and structural data in the Venafro intermontane basin (Central-Southern Apennines, Italy). *Geomorphology*, 283:80–101.
- Armas, I. (2008). Social vulnerability and seismic risk perception. Case study: the historic center of the Bucharest Municipality/Romania. *Natural Hazards*, pages 397–410.
- Armas, I. and Gavris, A. (2016). Census-based social vulnerability assessment for Bucharest. In *International Conference – Environment at a Crossroads: SMART approaches for a sustainable future*.

- Attema, E., Desnos, Y. L., and Duchossois, G. (2000). Synthetic aperture radar in Europe: ERS, Envisat, and beyond. *Johns Hopkins Apl Technical Digest*.
- A.U.TH. (1981). Permanent Regional Seismological Network operated by the Aristotle University of Thessaloniki, doi:10.7914/sn/ht.
- Benekos, G., Derdelakos, K., Bountzouklis, C., and Parcharidis, I. (2014). Monitoring the subsidence in the plain of south Thessaly with SAR interferometry. In *10th International Geographical Congress of Hellenic Geographical Society*.
- Berardino, P., Fornaro, G., Lanari, R., and Sansosti, E. (2002). A New Algorithm for Surface Deformation Monitoring Based on Small Baseline Differential SAR Interferograms. *IEEE Transaction on geoscience and remote sensing*, 40(11).
- Burton, P. W., Xu, Y., Qin, C., Tselentis, G.-A., and Sokos, E. (2004). A catalogue of seismicity in Greece and the adjacent areas for the twentieth century. *Tectonophysics*, 390:117–127.
- Calvagnile, G., D’Ingeo, F., Farrugia, P., and Panza, G. F. (1982). The lithosphere in the central-eastern Mediterranean area. *pure and applied geophysics*.
- Casu, F. (2009). *The Small Baseline Subset technique: performance assessment and new developments for surface deformation analysis of very extended areas*. PhD thesis, Dept. of Electrical and Electronic Engineering University of Cagliari.
- Chen, C.-T., Hu, J.-C., Lee, C.-Y. L. J.-C., and Chan, Y.-C. (2007). Thirty-year land elevation change from subsidence to uplift following the termination of groundwater pumping and its geological implication in the metropolitan Taipei basin, northern Taiwan. *Engineering Geology*, pages 30–47.
- Cordonnier, G., Braun, J., Cani, M., Benes, B., Galin, E., Peytavie, A., and Guerin, E. (2016). Terrain Generation from Tectonic Uplift and Fluvial Erosion. *Eurographics*.
- Cornell, C. A. (1968). Engineering seismic risk analysis. *Bulletin of the Seismological Society of America*, 58(5):1583–1606.
- CRED (2015). The human cost of natural disasters - A global perspective. Report from: Center for Research on the Epidemiology of Disasters.

- Crosetto, M., Monserrat, O., Cuevas-Gonzaleza, M., Devanthery, N., and Crippa, B. (2016). Persistent scatterer interferometry: A review. *ISPRS Journal of Photogrammetry and Remote Sensing*, 115:78–89.
- Crosetto, M., Monserrat, O., Jungner, A., and Crippa, B. (2009). Persistent scatterer interferometry: Potential and limits. In *Conference: ISPRS Hannover Workshop 2009, High-Resolution Earth Imaging for Geospatial Information, At , Hannover, Germany*.
- DeZan, F. and Lopez-Dekker, P. (2011). Sar image stacking for the exploitation of long-term coherent targets. *IEEE Geoscience and Remote Sensing Letters*, 8:502 – 506.
- Doornhof, D., Kristioansen, T. G., Nagel, N. B., Pattillo, P. D., and Sayers, C. (2006). Compaction and Subsidence. *Oilfield Review*, 18.
- Doutsos, T., Kontopoulos, N., and Poulimenos, G. (1988). The Corinth-Patras rift as the initial stage of continental fragmentation behind an active island arc (Greece). *Basin Research*, 1:177–190.
- Doutsos, T. and Poulimenos, G. (1992). Geometry and kinematics of active faults and their seismotectonic significance in the western Corinth-Patras rift (Greece). *Journal of Structural Geology*, 14:689–699.
- Dubock, P., Spoto, F., Simpson, J., Spencer, D., Schutte, E., and Sontag, H. (2001). Reprint ESA Bulletin No. 106.
- Duchossois, G. and Martin, P. (1995). Ers-1 and ers-2 tandem operations.
- Duff, P. M. D. (1993). *Holme's principles of physical geology*. Stanley Thornes Ltd, fourth edition.
- Earle, S. (2015). *Physical Geology*. BC Earth Science Articulation Committee.
- El-Betar, S. A. (2016). Seismic vulnerability evaluation of existing R.C. buildings. *HBRC Journal*.
- Elias, P. (2013). *Ground deformation observed in the western Corinth rift (Greece) by means of SAR interferometry Defended*. PhD thesis.
- Elias, P., Kontoes, C., Sykioti, O., Avallone, A., VanGorp, S., Briole, P., and Paradissis, D. (2006). A method for minimising of low frequency and unwrapping artefacts from interferometric calculations. *International Journal of Remote Sensing*, 27(14):3079–3086.

- ESA (2016). ASAR Image Mode Single Look Complex. url: <https://earth.esa.int/web/guest/data-access/browse-data-products/-/article/asar-image-mode-single-look-complex-1616>, last accessed on 02/08/2017.
- ESA (2017a). ERS-1/2 - SAR Level 1 Single Look Complex Image Product . url: <https://earth.esa.int/web/guest/data-access/browse-data-products/-/article/sar-single-look-complex-image-product-1368>, last accessed on 15/08/2017.
- ESA (2017b). Interferometric wide swath. url: <https://sentinel.esa.int/web/sentinel/user-guides/sentinel-1-sar/acquisition-modes/interferometric-wide-swath>, last accessed on 28/09/2017.
- ESA (2017c). Introducing SENTINEL-1. url: <http://www.esa.int/Our-Activities/Observing-the-Earth/Copernicus/Sentinel-1/Introducing-Sentinel-1>, last accessed on 03/09/2017.
- Ferretti, A. (2014). *Satellite InSAR Data: Reservoir Monitoring from Space*. EAGE Publications bv.
- Ferretti, A., Monti-Guarnieri, A., Prati, C., Rocca, F., and Massonnet, D. (2007a). *InSAR Principles: Guidelines for SAR Interferometry Processing and Interpretation 2007 - Part A*. European Space Agency, karen fletcher edition.
- Ferretti, A., Monti-Guarnieri, A., Prati, C., Rocca, F., and Massonnet, D. (2007b). *InSAR Principles: Guidelines for SAR Interferometry Processing and Interpretation 2007 - Part B*. European Space Agency, karen fletcher edition.
- Ferretti, A., Monti-Guarnieri, A., Prati, C., Rocca, F., and Massonnet, D. (2007c). *InSAR Principles: Guidelines for SAR Interferometry Processing and Interpretation 2007 - Part C*. European Space Agency, karen fletcher edition.
- Ferretti, A., Prati, C., and Rocca, F. (2001). Permanent scatterers in sar interferometry. *IEEE Transactions on geosceince and remote sensing*, 39(1).
- Ferretti, A., Prati, C., Rocca, F., and Wasowski, J. (2006). Satellite interferometry for monitoring ground deformations in the urban environment. *The Geological Society of London. IAEG2006 Paper number 284*.
- Flotte, N., Sorel, D., Muller, C., and Tensi, J. (2005). Along strike changes in the structural evolution over a brittle detachment fault: Example of the Pleistocene Corinth Patras rift (Greece). *Tectonophysics*, 403:77–94.

- Ford, M., Rohais, S., Williams, E. A., Bourlange, S., Jousselin, D., Backert, N., and Malartre, F. (2013). Tectono-sedimentary evolution of the western Corinth rift (Central Greece). *Basin Research*, pages 3–25.
- Freire, S. and Aubrecht, C. (2012). Integrating population dynamics into mapping human exposure to seismic hazard. *Natural Hazards and Earth System Sciences*.
- Gaki-Papanastasiou, K., Papanastasiou, D., and Maroukian, H. (1996). Geomorphic and archaeological - historical evidence for past earthquakes in Greece. *Annali di Geofisica*, XXXIX(3).
- GAMMA (2013). *GMMA Software Introduction. Documentation - User's Guide*. GAMMA Remote Sensing AG, 1.1 edition.
- Girty, G. H. (2009). *Perilous Earth: Understanding Processes Behind Natural Disasters*. url: <http://www.geology.sdsu.edu/visualgeology/naturaldisasters/Chapters/Chapter5Faults.pdf>, last accessed on 14/10/2017.
- Gupta, I. D. (2007). Probabilistic seismic hazard analysis method for mapping of spectral amplitudes and other design-specific quantities to estimate the earthquake effects on man-made structures. *ISET journal of Earthquake Technology*, 44(480):127–167.
- Holzer, T. L. (1983). Subsidence of Land Caused by Ground-Water Pumping. In *Groundwater: Allocation, Development and Pollution (Summer Conference, June 6-9)*.
- Hooper, A., Bekaert, D., Spaans, K., and Arikan, M. (2012). Recent advances in SAR interferometry time series analysis for measuring crustal deformation. *Tectonophysics*, 514-517:1–13.
- I.G.M.E. (2017). Institute of geology & mineral exploration. url: <http://www.igme.gr/geoportal/>, last accessed on 04/08/2017.
- INSPIRE (2012). D2.8.II/III.4 INSPIRE Data Specification on Geology, Draft Guidelines. INSPIRE Thematic Working Group Geology.
- Intrieri, E., Gigli, G., Nocentini, M., Lombardi, L., Mugnai, F., Fidolini, F., and Casagli, N. (2015). Sinkhole monitoring and early warning: An experimental and successful GB-InSAR application. *Geomorphology*, 241:304–314.

- IRIS (2017). Fault: Oblique. url: <https://www.iris.edu/hq/inclass/animation/faultoblique>, last accessed on 18/10/2017.
- Jain, S. (2014). *Fundamentals of Physical Geology*. Springer.
- Kassaras, I., Kapetanidis, V., and Karakonstantis, A. (2016). On the spatial distribution of seismicity and the 3D tectonic stress field in western Greece. pages 50–72.
- Klemm, H., Quseimi, I., Novali, F., Ferretti, A., and Tamburini, A. (2010). Monitoring horizontal and vertical surface deformation over a hydrocarbon reservoir by PSInSAR. *first break volume 28*.
- Koukis, G., Sabatakakis, N., Tsiambaos, G., and Katrivesis, N. (2005). Engineering geological approach to the evaluation of seismic risk in metropolitan regions: case study of Patras, Greece. *Bulletin of Engineering Geology and the Environment*, 64:219–235.
- Kouskouna, V. and Makropoulos, K. (2004). Historical earthquake investigations in Greece. *Annals of geophysics*, 47(2/3).
- Kramer, H. J. (2017). EnviSat (Environmental Satellite). url: <https://directory.eoportal.org/web/eoportal/satellite-missions/e/envisat>, last accessed on 22/08/2017.
- Lanari, R., Casu, F., Manzo, M., Zeni, G., Berardino, P., Manunta, M., and Pepe, A. (2007). An Overview of the Small BAseline Subset Algorithm: A DInSAR Technique for surfasce Deformation Analysis. *Pure and Applied Geophysics*.
- Lee, F. T. and Abel Jr., J. F. (1983). Subsidence from Underground Mining: Environmental Analysis and Planning Considerations. *Gological survey circular 876*.
- Lee, W. H., Kanamori, H., Jennings, P., and Kisslinger, C. (2003). *International Handbook of Earthquake & Engineering Seismology, Part 2*.
- Manconi, A. (2017). Workshop: SBAS-DInSAR processing on the ESA GeoHazard Exploitation Platform. swissuniversities, European Space Agency, Institute for Electromagnetic Sensing of the Environment (IREA) and ETH Zurich.

- Mantyniemi, P., Tsapanos, T. M., and Kijko, A. (2004). An estimate of probabilistic seismic hazard for five cities in Greece by using the parametric-historic procedure. *Engineering Geology*, pages 217–231.
- Manunta, M. (2009). *New Advances in Multi-Temporal Differential SAR Interferometry for Full Resolution Data Analysis*. PhD thesis.
- Margaris, B., Papazachos, C., Papaioannou, C., Theodulidis, N., Kalogeras, I., and Skarlatoudis, A. (2002). Ground motion attenuation relations for shallow earthquakes in Greece. In *12th European Conference on Earthquake Engineering*, volume 385.
- Massonnet, D. and Feigl, K. L. (1998). *Radar interferometry and its application to changes in the Earth's surface*, volume 36, chapter Radar interferometry and its application to changes in the Earth's surface, pages 441–500. American Geophysical Union, 4 edition.
- McNeill, L. C., Mille, A., Minshull, T. A., Bull, J. M., Kenyon, N. H., and Ivanov, M. (2004). Extension of the North Anatolian Fault into the North Aegean Trough: Evidence for transtension, strain partitioning, and analogues for Sea of Marmara basin models. *Tectonics an AGU journal*, 23(2).
- Melis, N. S., Brooks, M., and Pearce, R. G. (1989). A microearthquake study in the Gulf of Patras region, western Greece, and its seismotectonic interpretation. *Geophysical Journal*, pages 515–524.
- M. Mucciarelli, P. Contri, G. Monachesi, G. Calvano, and M. Gallipoli (2001). An Empirical Method to Assess the Seismic Vulnerability of Existing Buildings Using the HVSR Technique. *Pure and applied geophysics*, 158:2635–2647.
- Molnar, P. (2015). *Plate Tectonics: A Very Short Introduction*. OUP Oxford.
- Moreira, A., Prats-Iraola, P., Younis, M., Krieger, G., Hajnsek, I., and Papathanassiou, K. P. (2013). *A Tutorial on Synthetic Aperture Radar*. Microwaves and Radar Institute of the German Aerospace Center (DLR), Germany. IEEE Geoscience and remote sensing magazine.
- Oral, M. B., Reilinger, R. E., M. Nafi Toksdz, R. W. . K., and Ibrahim Kinik, A. A. B., and Lenk, O. (1995). Global Positioning System Offers Evidence of Plate Motions in Eastern Mediterranean. *Eos, Transactions American Geophysical Union*.

- Osmanoglu, B., Sunar, F., Wdowinski, S., and Cabral-Cano, E. (2015). Time series analysis of InSAR data: Methods and trends. *ISPRS J. Photogram. Remote Sensing*.
- Ouchi, K. (2013). Recent Trend and Advance of Synthetic Aperture Radar with Selected Topics. *Remote Sensing*.
- Panza, G. F., Irikura, K., Kouteva-Guentcheva, M., Peresan, A., Wang, Z., and Saragoni, G. R. (2011). Advanced Seismic Hazard Assessment. *Pure and Applied Geophysics*.
- Papadopoulos, G. A. and Arvanitides, A. (1996). *Earthquake Risk Assessment in Greece*, pages 221–229.
- Papanikolaou, D. . (2009). Timing of tectonic emplacement of the ophiolites and terrane paleogeography in the Hellenides. *Lithos*, 108:262–280.
- Papanikolaou, I. and Lekkas, E. (2008). Lithostratigraphic differentiation of the Gavrovo and Ionian flysch in the Southern Akarnania and the role of the Evinos and Agrilia transverse fault zones. *Hellenic Journal of Geosciences(former Ann. Geol. Pays Hellen*.
- Parcharidis, I., Foumelis, M., Kourkouli, P., and Wegmuller, U. (2009a). Persistent Scatterers InSAR to detect ground deformation over Rio-Antirio area (Western Greece) for the period 1992-2000. *Journal of Applied Geophysics*, 68:348–355.
- Parcharidis, I., Kokkalas, S., Fountoulis, I., and Foumelis, M. (2009b). Detection and Monitoring of Active Faults in Urban Environments: Time Series Interferometry on the Cities of Patras and Pyrgos (Peloponnese, Greece). *Remote sensing*, 1:676–696.
- Plag, H.-P., Ambrosius, B., Baker, T., Beutler, G., Bianco, G., Blewitt, G., Boucher, C., Davis, J., Degnan, J., Johansson, J., Kahle, H.-G., Kumkova, I., Marson, I., Mueller, S., Pavlis, E., Pearlman, M., Richter, B., Spakman, W., Tatevian, S., Tomasi, P., Wilson, P., and Zerbini, S. (1998). Scientific objectives of current and future WEGENER activities. *Tectonophysics*, pages 177–223.
- Qu, F., Lu, Z., Zhang, Q., Bawden, G. W., Kim, J.-W., Zhao, C., and Qu, W. (2015). Mapping ground deformation over Houston–Galveston, Texas using multi-temporal InSAR. *Remote Sensing of Environment*, 169:290–306.

- Raucoules, D., deMichele, B. B. M., LeCozanet, G., Closset, L., Bremmer, C., Veldkamp, H., Tragheim, D., Bateson, L., Crosetto, M., and Agudo, M. (2007). Persistent Scatterers Interferometry Independent Validation and Intercomparison of Results – Final Report. BRGM/RP-55649-FR.
- Robertson, A. and Shallo, M. (2000). Mesozoic–Tertiary tectonic evolution of Albania in its regional Eastern Mediterranean context. *Tectonophysics*, pages 197–254.
- Rontogianni, S. (2010). Comparison of geodetic and seismic strain rates in Greece by using a uniform processing approach to campaign GPS measurements over the interval 1994 - 2000. *Journal of Geodynamics*, pages 381–399.
- Rosen, P. (2011). Principles and Theory of Radar Interferometry. NASA. Jet Propulsion Laboratory.
- Rozos, D., Koukis, G., and Sabatakakis, N. (2006). Large-scale engineering geological map of the Patras city wider area, Greece. *The Geological Society of London*.
- Sakkas, V., Adam, N., Papadimitriou, P., Voulgaris, N., Vassilopoulou, S., Damiata, B. N., Lagios, E., and Stramondo, S. (2013). Combined Ground Deformation Study Of Broader Area Of Patras Gulf (W. Greece) Using PSI-WAP, DGPS And Seismicity Analyses. In *Conference: ESA Living Planet Symposium 2013, At Edinburgh*.
- Samieie-Esfahany, S., Hanssen, R. F., van Thienen-Visser, K., and Muntendam-Bos, A. (2009). On the effect of horizontal deformation on insar subsidence estimates. In *Fringe 2009, Proceedings of the workshop Held 30 November - 4 December 2009, in Frascati, Italy.*, volume 677.
- Schmullius, C. (2017). Echoes in space - History. url: <https://eo-college.org/courses/echoes-in-space/>, last accessed on 10/10/2017.
- Simons, M. and Rosen, P. A. (2007). *Treatise on Geophysics*, chapter Interferometric Synthetic Aperture Radar Geodesy, pages 391–446. Elsevier.
- Sipos, T. K. and Hadzima-Nyarko, M. (2017). Rapid seismic risk assessment. *International Journal of Disaster Risk Reduction*, 24:348–360.
- Sitharam, T. G. and Anbazhagan, P. (2007). Seismic Hazard Analysis for the Bangalore Region. *Natural Hazards*, 40(2):261–278.

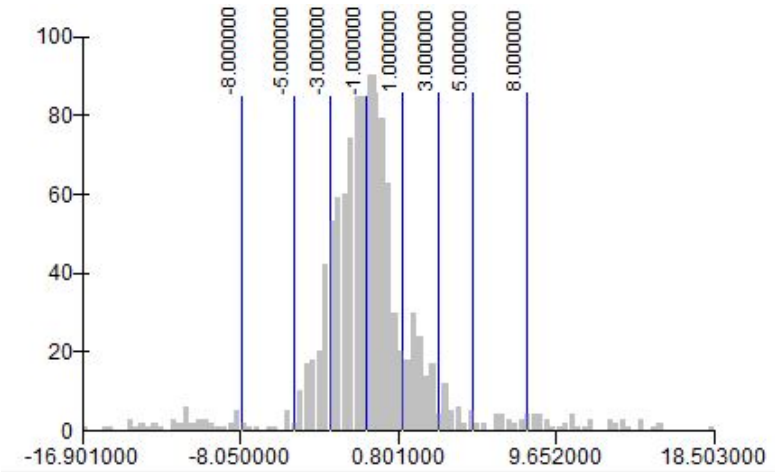
- Solomos, G., Pinto, A., and Dimova, S. (2008). A review of the seismic hazard zonation in national building codes in the context of EUROCODE 8. Technical report, EUR - Scientific and Technical Research Reports.
- Sousa, J. J. and Bastos, L. (2013). Multi-temporal SAR interferometry reveals acceleration of bridge sinking before collapse. *Natural Hazards and Earth System Sciences*.
- Strozzi, T., Wegmuller, U., Werner, C., and Wiesmann, A. (2000). Measurement of slow uniform surface displacement with mm/year accuracy. In *IGARSS 2000. IEEE 2000 International Geoscience and Remote Sensing Symposium. Taking the Pulse of the Planet: The Role of Remote Sensing in Managing the Environment. Proceedings (Cat. No.00CH37120)*, volume 5, pages 2239–2241.
- Sylvester, A. (1988). Strike-Slip Faults. *Geological Society of America Bulletin*, pages 1666–1703.
- Tompolidi, A. (2017). Observation of urban faults by using space geodesy: The case of the city of Corinth. Master's thesis, Harokopio University. Department of Geography.
- Tsapanos, T. M. (2008). *Seismicity and Seismic Hazard Assessment in Greece*, pages 253–270.
- Tsapanos, T. M., Mantyniemi, P., and Kijko, A. (2004). A probabilistic seismic hazard assessment for Greece and the surrounding region including site-specific considerations. *Annals of geophysics*, 47(6).
- Tselentis, G.-A., Serpetsidaki, A., Gkika, F., E.Sokos, Danciu, L., and Paraskevopoulos, P. (2004). *Seismic Hazard Simulation And Risk Reduction Training Algorithm For The City Of Patras-Greece*, volume 77, pages 12–22.
- Tsipianitis, A. D. (2015). Improvement of regional seismic hazard assesment considering active faults. Master's thesis.
- Usai, S. (2003). A Least Squares Database Approach for SAR Interferometric Data. *IEEE Transaction in geoscience and remote sensing*, 41(4).
- USGS (2017). USGS Earth Explorer. url: <https://earthexplorer.usgs.gov/>, last accessed on 04/10/2017.
- Van-Zyl, J. (2017). Radar Interferometry Basics, EE/Ae 157, Introduction to the Physics of Remote Sensing, Caltech Institute.

- Van't-Klooster, C. G. M. (2011). ERS-1, European Remote-Sensing Satellite Was Launched 20 Years Ago.
- Vasile, G. and Besic, N. (2013). Fundamentals of Remote Sensing: SAR Polarimetry. GIPSA-lab.
- Veci, L. (2016a). *Sentinel-1 Toolbox Interferometry Tutorial*. Array Systems Computing Inc. and ESA, second edition.
- Veci, L. (2016b). *Sentinel-1 Toolbox TOPSAR Interferometry Tutorial*. Array Systems Computing Inc. and ESA, second edition.
- Vervoort, A. and Declercq, P.-Y. (2018). Upward surface movement above deep coal mines after closure and flooding of underground workings. *International Journal of Mining Science and Technology*, 28:53–59.
- Wang, Z. (2008). Understanding seismic hazard and risk: a gap between engineers and seismologists. In *The 14th world conference on earthquake engineering*.
- Wang, Z. (2009a). Seismic Hazard and Risk Analyses: Issues and Alternatives. In *Joint ICTP/IAEA Advanced Workshop on Earthquake Engineering for Nuclear Facilities*.
- Wang, Z. (2009b). Seismic Hazard vs. Seismic Risk. *Seismological Research Letters*, 80:673–674.
- Werner, C., Wegmuller, U., Strozzi, T., and Wiesmann, A., editors (2003). *Interferometric point target analysis for deformation mapping*. Geoscience and Remote Sensing Symposium, 2003. IGARSS '03. Proceedings. 2003 IEEE International.
- Wessels, J. (2017a). *InSAR User Manual Geomatica 2017*. PCI Geomatics.
- Wessels, J. (2017b). *InSAR User Manual Geomatica 2017*. PCI Geomatics, 1.1 edition.
- Wieland, M., Pittore, M., Parolai, S., and Zschau, J. (2012). Exposure Estimation from Multi-Resolution Optical Satellite Imagery for Seismic Risk Assessment. *ISPRS International Journal of Geo-Information*, pages 69–88.
- Williams, S., Bock, Y., and Fang, P. (1998). Integrated satellite interferometry: Tropospheric noise, GPS estimates and implications for interferometric synthetic aperture radar products. *Journal Of Geophysical Research: Solid Earth*, 103:27051–27067.

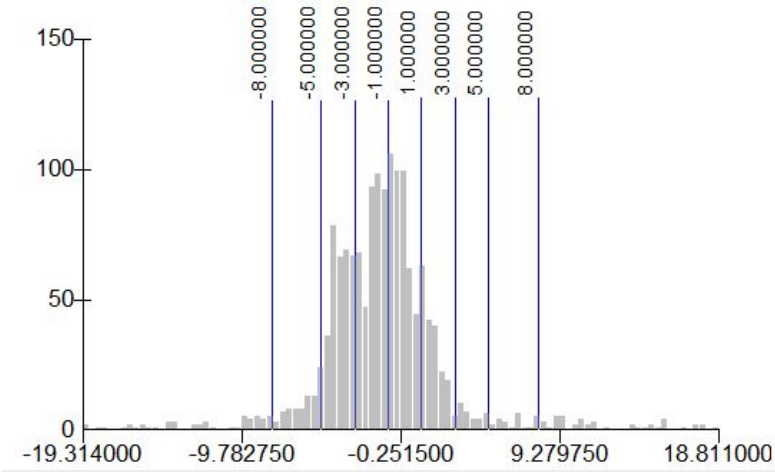
- Woodside, J. M. (1977). Tectonic elements and crust of the eastern Mediterranean Sea. *Marine Geophysical Researches*, 3(3):317–354.
- Yamin, L. E., Hurtado, A., Rincon, R., Dorado, J. F., and Reyes, J. C. (2017). Probabilistic seismic vulnerability assessment of buildings in terms of economic losses. *Engineering Structures*, 138:308–323.
- Yucel, G. and Arun, G. (2012). Earthquake and Physical and Social Vulnerability Assessment for Settlements: Case Study Avcilar District. In *15th World Conference on Earthquake Engineering*.
- Zebker, H. A. and Villasenor, J. (1992). Decorrelation in Interferometric Radar Echoes. *IEEE TRANSACTIONS ON GEOSCIENCE AND REMOTE SENSING*, 3(5).

Appendices

A ERS data frequencies



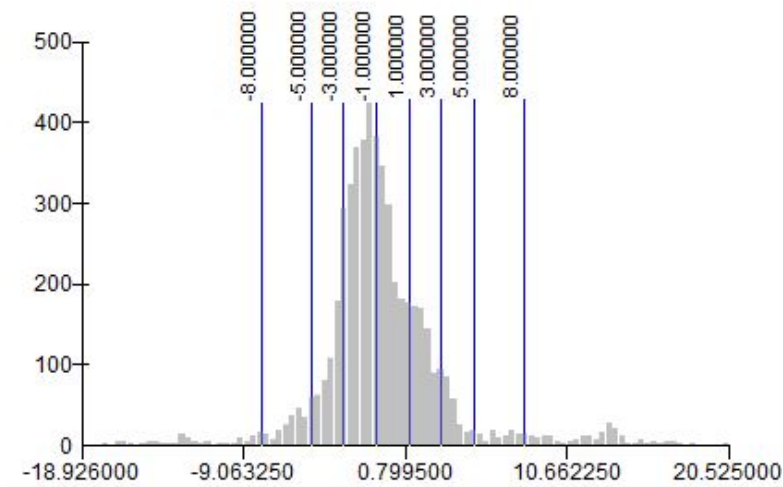
(a) descending



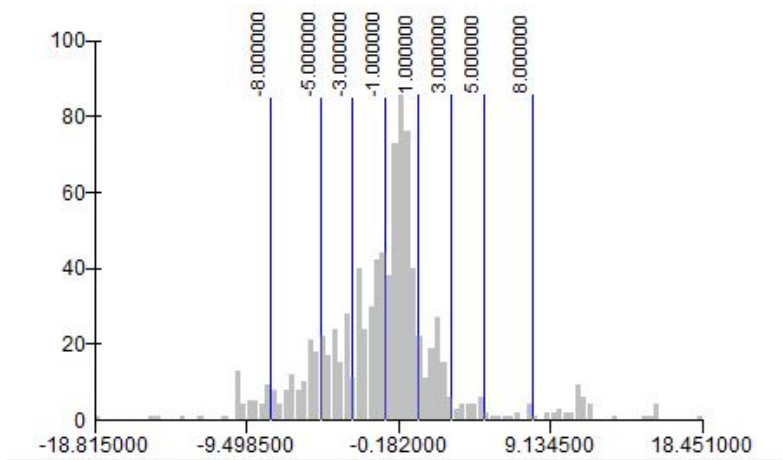
(b) ascending

Figure 31: Histograms of ground motion from ERS data analysis. Frequency is marked on the Y axis, millimeter values on the X axis. The vertical lines indicate important value ranges.

B Envisat data frequencies



(a) descending



(b) ascending

Figure 32: Histograms of ground motion from Envisat data analysis. Frequency is marked on the Y axis, millimeter values on the X axis. The vertical lines indicate important value ranges.

C TerraSAR-X data frequencies

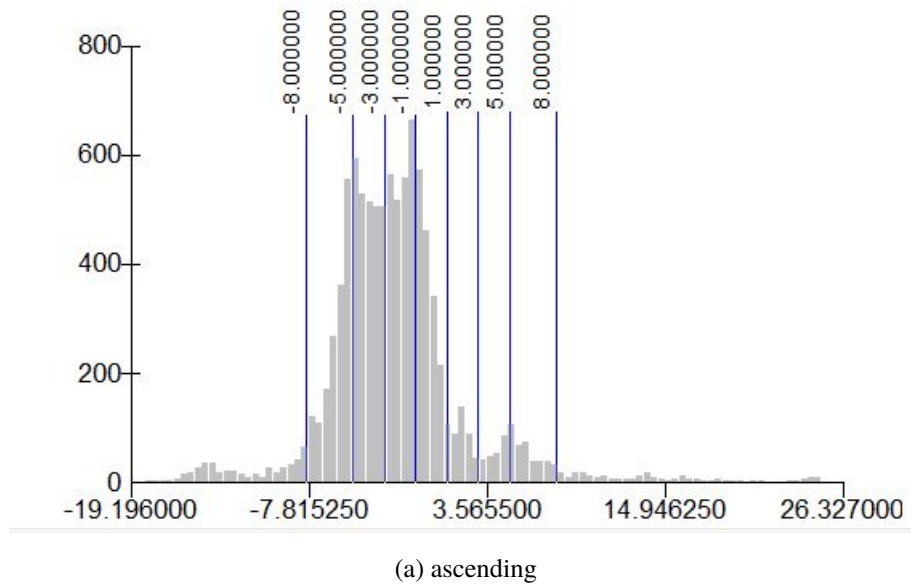
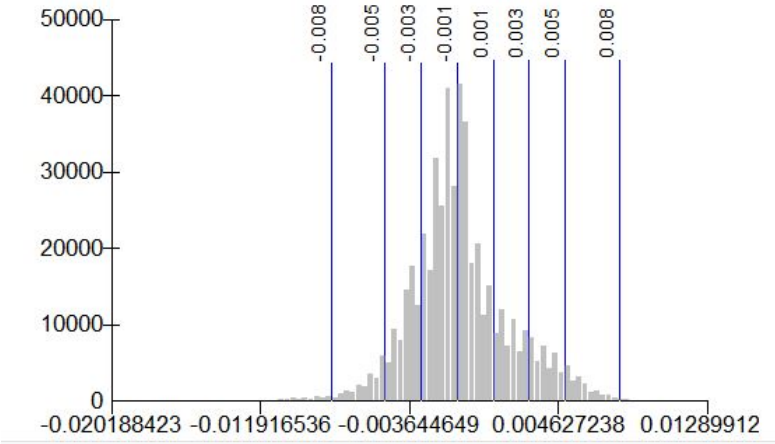
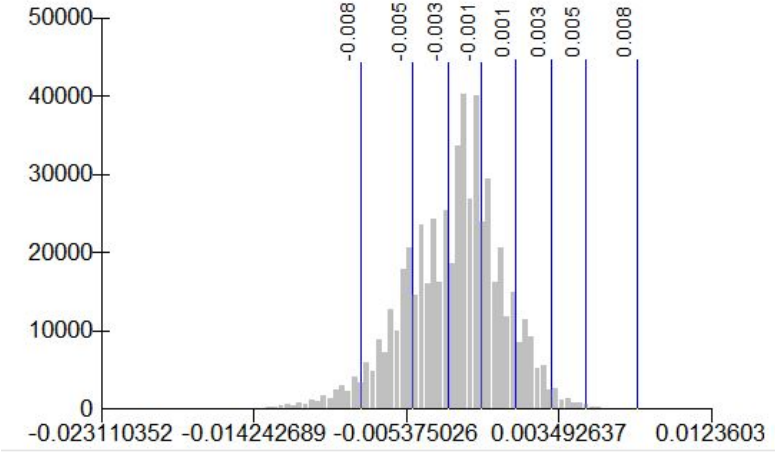


Figure 33: Histogram of ground motion from TerraSAR-X data analysis. Frequency is marked on the Y axis, millimeter values on the X axis. The vertical lines indicate important value ranges.

D Sentinel-1 data frequencies



(a) descending



(b) ascending

Figure 34: Histograms of ground motion from Sentinel-1 data analysis. Frequency is marked on the Y axis, meter values on the X axis. The vertical lines indicate important value ranges.